

1 **Simulations of gravitoelastic correlations for the**
2 **Sardinian candidate site of the Einstein Telescope**

3 **Tomislav Andric^{1,2} and Jan Harms^{1,2}**

4 ¹Gran Sasso Science Institute (GSSI), I-67100 L'Aquila, Italy
5 ²INFN, Laboratori Nazionali del Gran Sasso, I-67100 Assergi, Italy

6 **Key Points:**

- 7 • Spectral-element simulation can be used to calculate gravitoelastic correlations
8 of ambient seismic fields
9 • Topography at Sardinian candidate site of Einstein Telescope has significant im-
10 pact on gravitoelastic correlations
11 • Topography at Sardinian site acts as low-pass filter for Rayleigh waves

Corresponding author: Tomislav Andric, tomislav.andric@gssi.it

Abstract

Gravity fluctuations produced by ambient seismic fields are predicted to limit the sensitivity of the next-generation, gravitational-wave detector Einstein Telescope at frequencies below 20 Hz. The detector will be hosted in an underground infrastructure to reduce seismic disturbances and associated gravity fluctuations. Additional mitigation might be required by monitoring the seismic field and using the data to estimate the associated gravity fluctuations and to subtract the estimate from the detector data, a technique called coherent noise cancellation. In this paper, we present a calculation of correlations between surface displacement of a seismic field and the associated gravitational fluctuations using the spectral-element SPECFEM3D Cartesian software. The model takes into account the local topography at a candidate site of the Einstein Telescope at Sardinia. This paper is a first demonstration of SPECFEM3D’s capabilities to provide estimates of gravitoelastic correlations, which are required for an optimized deployment of seismometers for gravity-noise cancellation.

1 Introduction

A next generation of ground-based, gravitational-wave (GW) observatories has been proposed including the European concept Einstein Telescope (ET) (ET Science Team, 2011), and the US concepts Voyager (Adhikari et al., 2020) and Cosmic Explorer (Reitze et al., 2019). These detectors would have greatly improved sensitivity over almost the entire GW observation band compared to current-generation detectors Virgo (Acernese et al., 2015), LIGO (Abbott et al., 2016), KAGRA (Akutsu et al., 2019), and LIGO India (Souradeep, 2016). Terrestrial gravity noise, also known as Newtonian noise (NN), constitutes one of the fundamental infrastructure limitations, which affects the sensitivity of GW detectors. NN originates from density fluctuations in the surrounding ground and atmosphere, causing a variation in the gravitational field and these gravity fluctuations act on the test masses (TM) causing detector noise mostly below 30 Hz (Harms, 2019). A large sensitivity improvement is targeted with ET in the infrasound observation band (1 to 20 Hz), where current generations of detectors have no detection capabilities. This will increase the number and signal-to-noise ratio of observable GW signals and therefore significantly enhance the astrophysical impact of third-generation observatories (Hild et al., 2011; Maggiore et al., 2020). In the frequency band below 30 Hz, it is possible to follow better the inspiral phase of compact binaries composed of neutron stars (NS) and stellar-mass black holes (BH), or open the window to observations of intermediate-mass black holes (IMBH). It is possible to follow the waveform evolution for a longer amount of time and this practically means: more accurate estimates of some of the binary system’s parameters including its sky location (Grimm & Harms, 2020), and potentially an early warning for the electromagnetic (EM) follow-up of these sources (Chan et al., 2018). Einstein Telescope will also be sensitive to continuous GW emission from a large population of spinning NSs below 10 Hz (Sathyaprakash et al., 2012). Therefore, there is a strong scientific drive to expand the detection band and to improve the sensitivity down to lower frequencies.

The dominant noise sources at very low frequencies are those associated with the seismic motion that couples with the detector. One mechanism is the mechanical transmission, where ground vibrations perturb the motion of the TM via the TM suspension system. This is known as seismic noise. Elaborated vibration-isolation systems are used to suspend the TM, significantly reducing seismic disturbances within the detection band (Acernese et al., 2010; Matichard et al., 2014). Another mechanism is by gravitational coupling giving rise to NN and cannot be shielded in any way (M. Beker et al., 2011; M. G. Beker et al., 2015). A well-explored cancellation scheme is based on Wiener filters (Cella, 2000; Badaracco & Harms, 2019; M. Coughlin et al., 2016; M. W. Coughlin et al., 2018). Wiener filters are linear filters calculated from the correlation between the reference and target channels (Orfanidis, 2007). In the context of seismic NN cancellation, the sensors (seis-

64 mometers) monitor seismic fields, which means that correlations between them are to
 65 be expected (Harms, 2019).

66 Most of the seismic noise is generated near the surface and it generally decreases
 67 significantly with depth. Predictions based on a detailed characterization of the LIGO
 68 sites show that seismic surface fields give the dominant contribution to NN (Driggers et
 69 al., 2012). Accordingly, a NN cancellation scheme can be realized using an array of seis-
 70 mometers deployed at the surface near the TM (M. Coughlin et al., 2016). The construc-
 71 tion of ET has been proposed to be underground, where the amount of seismic motion
 72 is expected to be lower and more stable (Harms et al., 2010; M. G. Beker et al., 2015;
 73 Mandic et al., 2018). NN is about two orders of magnitude less underground which is
 74 substantial (Amann et al., 2020).

75 One of the most important things in NN cancellation is the homogeneity of the seis-
 76 mic field. Scattering of seismic fields from an irregular surface topography can cause het-
 77 erogeneity of the seismic field. It can lead to a more complex field structure that is not
 78 completely characterized by surface displacement and will likely pose a great challenge
 79 even to 3D seismic surveys with boreholes where effective placement of seismometers needs
 80 to be achieved (Badaracco & Harms, 2019). The scattering will especially be the prob-
 81 lem if it is strong enough to alter seismic waveforms significantly over very short prop-
 82 agation distances (Driggers et al., 2012). Even if it is identified and fully characterized,
 83 scattering could pose a serious challenge to NN subtraction, since it might increase the
 84 required effort and therefore cost of a NN mitigation system. Issues of topographic scat-
 85 tering and its connection to NN cancellation are partly examined in (M. Coughlin & Harms,
 86 2012). They found that the total contribution of waves scattered from topography can
 87 be high, which makes topographic scattering relevant to NN subtraction in future low-
 88 frequency GW detectors. Seismic scattering was investigated analytically in numerous
 89 publications, see for example (Gilbert & Knopoff, 1960; Abubakar, 1962, 1963; J. A. Hud-
 90 son, 1967; Ogilvy, 1987). An extensive and conclusive study of the impact of topogra-
 91 phy scattering on coherent cancellation has not been carried out so far.

92 In this paper, we simulate synthetic ambient-noise cross-correlations between sta-
 93 tions at the surface of a finite-element model using a 3D spectral-element method (SEM)
 94 implemented in SPECFEM3D Cartesian software (Komatitsch & Tromp, 2002a, 2002b;
 95 Komatitsch et al., 2018). Cross-correlations are simulated for the flat model and for the
 96 topographic model using elevation data at the three (foreseen) vertices of the proposed
 97 ET site at Sardinia. Using these correlations we show the effects of topographic scatter-
 98 ing on seismic coherence and on correlations between test mass acceleration and verti-
 99 cal seismic surface displacement. These correlations are crucial in Wiener-filter construc-
 100 tion. One of the main goals in the future will be to investigate whether high noise can-
 101 cellation through Wiener filtering or similar methods will be effective at the Sardinia site
 102 for ET.

103 In section 2, the ET detector and the ET candidate site at Sardinia are briefly pre-
 104 sented. In section 3, our main analysis tools SPECFEM3D Cartesian and Trelis are in-
 105 troduced. In section 4, the building of the finite-element model is described. In section
 106 5, the theory of noise cross-correlation is reviewed with focus on the method implemented
 107 in SPECFEM3D. In section 6, ensemble sensitivity kernels and their importance are ex-
 108 plained. In section 7, we present the main results of our study concerning the effect of
 109 topographic scattering on seismic correlations and the prediction of gravitational cou-
 110 pling between seismic surface displacement and an underground test mass.

111 2 Einstein Telescope and Sardinia site

112 The third-generation GW observatory, ET, will be aiming to reach a sensitivity for
 113 GW signals emitted by astrophysical and cosmological sources about a factor of 10 bet-

114 ter than current detectors over much of the observation band. The targeted observation
 115 band is from 3 Hz to a few kHz with a strain sensitivity of about $10^{-24} \text{ Hz}^{-\frac{1}{2}}$ within this
 116 band (ET Science Team, 2011; Hild et al., 2011). As all of the GW detectors so far, ET
 117 will be a modified Michelson interferometer with suspended mirrors that act as TMs. These
 118 instruments behave as transducers to convert the space-time strain caused by a GW to
 119 fluctuations in optical power (Barsotti et al., 2019). In its final construction stage, ET
 120 should consist of three nested detectors, built a few 100 m underground, which would be
 121 arranged in a triangular pattern. Advantages of ET with respect to the traditional L-
 122 shaped geometry of current GW detectors are that it will have a more uniform antenna
 123 pattern and be sensitive to both GW polarizations independent of the wave-propagation
 124 direction. Each individual detector will comprise two interferometers forming a so-called
 125 xylophone configuration (Hild et al., 2009), one specialized for detecting low-frequency
 126 GWs (low laser power, low temperature; frequency range from 3 Hz to 50 Hz) and the
 127 other one for the high-frequency part (room temperature, high laser power, frequency
 128 range from 50 Hz to 10 kHz).

129 For the reduction of NN, a detector site with weak gravity fluctuations should be
 130 chosen. High-frequency seismic spectra (above a few Hz) are all significantly quieter un-
 131 derground than at typical surface sites (Harms et al., 2010; M. G. Beker et al., 2015; Mandic
 132 et al., 2018). This can be explained by the exponential fall of Rayleigh-wave amplitudes
 133 combined with the fact that high-frequency seismicity is typically generated at the sur-
 134 face, and most surface sites are covered by a low-velocity layer of unconsolidated ground.
 135 Also, underground sites are attractive since the risk that anthropic seismic noise will change
 136 in the future due to surface infrastructural developments like the construction of indus-
 137 try or traffic roads is lower (M. G. Beker et al., 2015). Additionally, atmospheric grav-
 138 ity perturbations are strongly suppressed underground (Fiorucci et al., 2018).

139 The selected site should offer the possibility for efficient coherent cancellation of
 140 NN with surface and borehole seismometer deployment. Two-point spatial correlation
 141 of the seismic field determines the efficiency of a cancellation scheme. The strongest scat-
 142 terer of seismic waves above a few Hz is the surface with rough topography (strong to-
 143 pographic gradients). If scattering is significant then correlation can be strongly altered,
 144 and a seismic array consisting of a potentially large number of seismometers needs to be
 145 deployed with difficult to determine sensor positions (Harms, 2019). Since the ground
 146 medium close to the TM at the Sardinia site is fairly uniform, high scattering cross sec-
 147 tions are unlikely to be observed for underground propagation of seismic waves (Driggers
 148 et al., 2012). Still, heterogeneity of the ground may add complexity, and a refined model
 149 should include information about local geology.

150 The suggested site at Sardinia (Italy) is near the city Lula (figure 1) with vertex
 151 coordinates given in table 1. Spectral density of the Sardinia site ambient seismic field
 152 is close to Peterson’s New Low Noise Model (NLNM) and there is no strong daily or sea-
 153 sonal variation above a few Hz (M. G. Beker et al., 2012, 2015). Also, what goes in fa-
 154 vor of the Sardinia site is the fact that the most seismically quiet sites are found in hard
 155 rock geologies and the Sardinia site is mostly made of granite and schist. In terms of the
 156 construction of underground facilities, rock stability is a crucial factor, which then tends
 157 to be more favorable in hard rock (M. G. Beker et al., 2015). This is disadvantageous
 158 for NN reduction with depth, which decreases exponentially with increasing seismic-wave
 159 speed. Coordinates of vertices were chosen taking into consideration the quality of the
 160 rocks.

161 These vertices make an equilateral triangle with approximately 10.7 km side length.
 162 Surface areas of $3 \text{ km} \times 3 \text{ km}$ size with topographies where the respective ET vertex is
 163 located under the center point of the area are given in figure 2. The resolution of ele-
 164 vation data is 30 m. For examination of seismic coherence and gravity-displacement cor-
 165 relations, due to high computational costs (and, for this study at least, due to limited
 166 computational resources of only about 100 nodes), we chose only vertex A3 because it

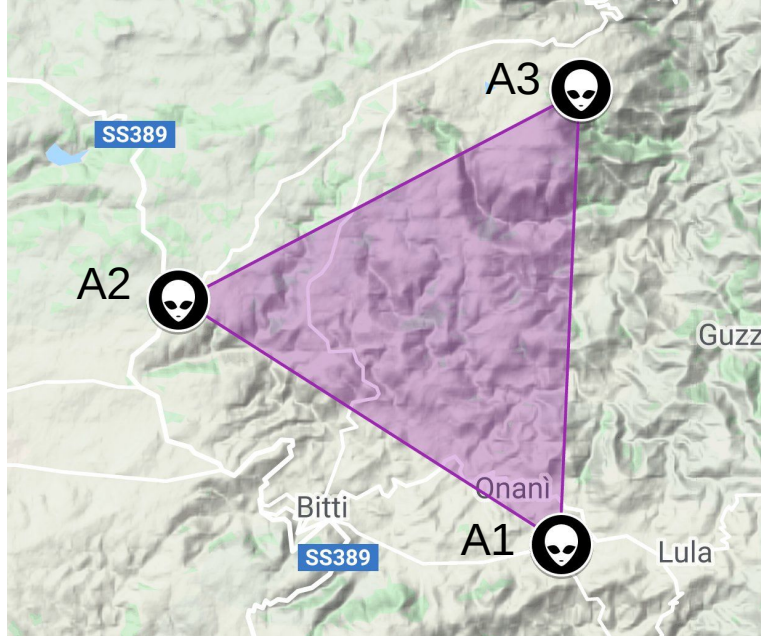


Figure 1: Sardinia candidate site for Einstein Telescope with marked vertex locations.

Cavern	Latitude	Longitude
A	40°28'21.11"	9°27'18.78"
B	40°31'27.73"	9°20'54.84"
C	40°34'08.24"	9°27'38.82"

Table 1: Coordinates of vertices of Einstein Telescope.

167 has the roughest surrounding topography (figure 2c) among all three vertices and there-
 168 fore the largest scattering potential. Roughness can for example be quantified by the rms
 169 of the elevation data, which are 52.4 m, 43.5 m, 129.6 m for the vertices A1, A2, A3, re-
 170 spectively. As already said, scattering causes heterogeneity of the seismic field, which
 171 will be one of the main problems in NN cancellation. If the problem of NN description
 172 and cancellation is understood for vertex A3, there will not be any additional challenges
 173 when repeating the analysis for vertices A1 and A2.

174 3 Finite-element simulation and model meshing

175 SPEC3D Cartesian is a powerful software package for seismic-wave propaga-
 176 tion modeling at local and regional scales based upon the spectral-element method (SEM)
 177 (Komatitsch & Tromp, 1999; Komatitsch et al., 1999). The SEM is a highly accurate
 178 numerical method, which combines the geometrical flexibility of the finite-element method
 179 with the fast convergence associated with spectral techniques, and it has origins in com-
 180 putational fluid dynamics (Patera, 1984; Maday & Patera, 1989; Seriani & Priolo, 2012).
 181 It uses a mesh of hexahedral finite elements on which the wave field is represented in terms
 182 of high-degree Lagrange polynomials on Gauss–Lobatto–Legendre interpolation points.
 183 SEM is more accurate than widely used classical techniques such as the finite-difference

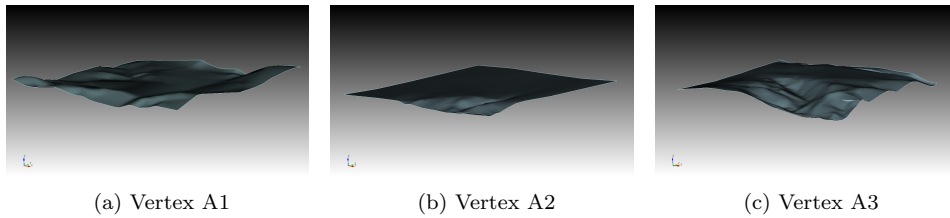


Figure 2: Elevation data at the three vertex locations of Einstein Telescope over areas with 3 km side lengths.

184 method (Virieux, 1986; Olsen et al., 1997), in particular for surface waves (Komatitsch
 185 & Tromp, 1999, 2002a), which play an important role in ground-motion seismology (Komatitsch,
 186 2004). It is also very well suited to parallel implementation on supercomputers and clus-
 187 ters of CPUs or GPUs (Komatitsch et al., 2003, 2008; Tsuboi et al., 2003). SPECFEM3D
 188 software is written in Fortran2003 with full portability in mind (Komatitsch et al., 2018).
 189 The package uses the parallel algorithm based upon the Message Passing Interface (MPI)
 190 (Gropp et al., 1994; Pacheco, 1997).

191 We used Trelis for the creation of models and their exporting into a SPECFEM3D
 192 Cartesian file format. Trelis is a full-featured software for generation of two- and three-
 193 dimensional finite-element grids (meshes) and geometry preparation (Blacker et al., 2019).
 194 Generating meshes for complex model-based geometries requires a variety of tools and
 195 many of them in Trelis are completely automatic. In creating a load-balanced, partitioned
 196 mesh, it is needed to set up a hexahedral mesh, in which goes a large amount of work,
 197 then to export that mesh into a SPECFEM3D Cartesian file format and to partition it
 198 for a chosen number of cores in SPECFEM3D. The next step is creating the distributed
 199 databases in which all the missing information needed by the SEM solver are created.
 200 The final step is to run the solver (Komatitsch et al., 2018). Creating the databases and
 201 running the solver in SPECFEM3D is done on parallel on a number of cores chosen while
 202 partitioning.

203 Besides earthquake simulations, SPECFEM3D Cartesian includes functionality for
 204 seismic noise tomography as well. It can perform noise cross-correlation simulations. At
 205 the end of noise cross-correlation simulations, two outputs are the most interesting: the
 206 simulated ensemble cross-correlations and the so-called ensemble sensitivity kernels, which
 207 quantify how much a correlation depends on properties of the ground medium through-
 208 out the model. Cross-correlations are generated based on a SEM (Komatitsch & Vilotte,
 209 1998; Komatitsch & Tromp, 1999) and ensemble finite-frequency sensitivity kernels are
 210 generated based on an adjoint method (Tromp et al., 2005; Liu & Tromp, 2008).

211 4 Model setup

212 Before running simulations using created models, a time-consuming step is to set
 213 up appropriate absorbing boundary conditions. In order to simulate a semi-infinite medium,
 214 absorbing conditions are used on all sides of the model except the free surface. If absorb-
 215 ing boundary conditions are not good enough there are significant artificial boundary
 216 reflections from the numerical model which affect cross-correlations. The convolutional
 217 perfectly matched layers (C-PML) absorbing boundary condition is very efficient from
 218 a numerical point of view for the elastic-wave equation in absorbing body waves with
 219 non-grazing incidence and surface waves (Komatitsch & Martin, 2007). C-PML has bet-
 220 ter absorbing efficiency, especially in the case of small mesh size, than commonly used

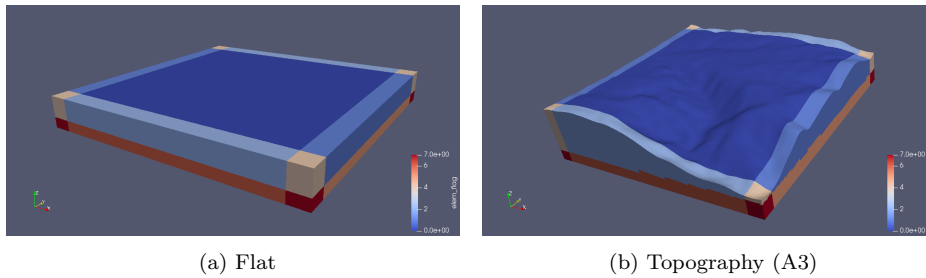


Figure 3: Models with convolutional perfectly matched boundary layers (C-PML).

221 Clayton-Enquist absorbing boundary conditions which are mostly sufficient in the case
 222 of large mesh size (Komatitsch, 2004).

223 In order to create quality absorbing boundary layers out of the edge elements/layers
 224 of the meshed model, it is important to have those elements/layers as regular as possi-
 225 ble with constant thickness and aligned with the coordinate grid axes (X, Y and/or Z).
 226 The thickness of C-PMLs can be different for the X, Y and Z sides, but must have a fixed,
 227 specific value for each coordinate individually. Usually, three or four C-PMLs on each
 228 of five absorbing model surfaces are sufficient, but as simulations showed, having more
 229 C-PMLs on each of the absorbing surfaces suppressed reflections more, regardless of the
 230 thickness of the single C-PML. A C-PML is very efficient but it does not absorb inci-
 231 dent waves completely (see figure 7). In order to prevent remaining parasitic waves to
 232 affect cross-correlations i. e. to reach receivers, simulation time is set to be quite low (0.94
 233 s). The thickness of the overall C-PML used for the flat surface model is 210 m, 210 m,
 234 120 m for the X, Y and Z boundary planes, respectively (figure 3a), and for the topog-
 235 raphy model 179 m, 174 m, 179 m (figure 3b). More information about C-PML can be
 236 found in (Martin & Komatitsch, 2009; Komatitsch & Martin, 2007; Martin et al., 2010;
 237 Xie et al., 2014).

238 The important parameter values of the model are $v_p = 3500$ m/s compressional-
 239 wave speed, $v_s = 2000$ m/s shear-wave speed, and $\rho = 2750$ kg/m³ for the uniform
 240 mass density based on the fact that at the suggested site, granite and partly schist pre-
 241vail, and also based on recent geoseismic studies (Giunchi et al., 2020). The simulations
 242 were performed without attenuation and anisotropy. We do not have any robust infor-
 243 mation about attenuation and anisotropy in this area yet. In addition, attenuation is not
 244 yet supported for noise cross-correlation simulations with SPECFEM3D. However, it can
 245 also be expected that attenuation plays a negligible role over the small extent of the medium
 246 relevant to gravity-noise calculations.

247 C-PML absorbing boundary condition is only supported in CPU mode for now (so
 248 one cannot use GPUs). Using GPUs would, of course, make the running of simulations
 249 much faster. Also, C-PML is still under test for the third step of cross-correlation sim-
 250 ulations – adjoint simulations.

251 The horizontal size of the models is 3 km × 3 km with a depth of 360 m in the flat
 252 free surface case (figure 4a) and with variable depth in the case with A3 topography. The
 253 minimum depth is 192 m and the maximum is 798 m (figure 4b). Mesh size of the flat
 254 free surface model is 30 m (for all three dimensions). For the topography model, it varies
 255 from 12 m to 71 m in Z dimension. For X and Y dimensions, it is 25 m. Mesh proper-
 256 ties play an important role in estimating the stability of the simulation and estimating
 257 the maximum frequency, up to which synthetics are valid. Stability of simulations de-
 258 pends on P-wave velocity, time step size and minimum distance between Gauss-Lobatto-

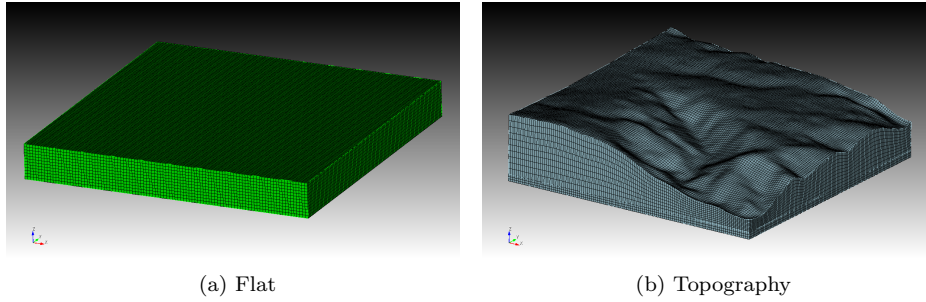


Figure 4: Meshed models.

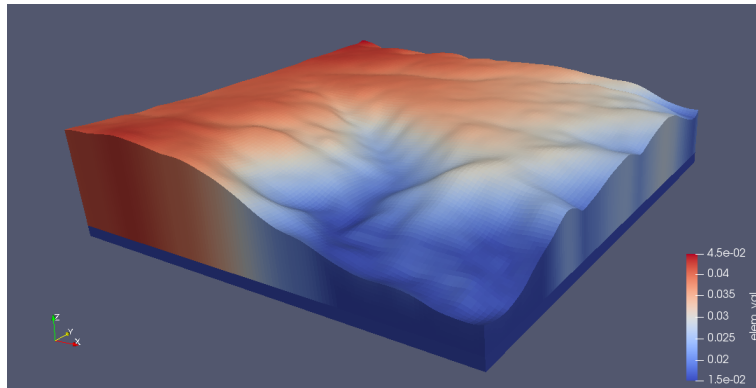


Figure 5: Minimum wave period resolved in each element of A3 topography model.

259 Legendre interpolation points. From these parameters, one can calculate the Courant
 260 number that is used as measure of stability of the simulation. We also made sure that
 261 the maximum frequency lies above the target band, i.e., above 30 Hz. Other important
 262 aspects of mesh design are governed by the meshing software Trelis.

263 As already said, the results of simulations are valid up to a certain maximum fre-
 264 quency (minimum period). This maximum frequency depends on the mesh size and S-
 265 wave velocity and for the flat, free surface model, it is 53 Hz (and it is constant through-
 266 out the model) and for the topography model it varies between 22 Hz and 66 Hz. Min-
 267 imum periods up to which simulations at the A3 vertex are valid in specific mesh ele-
 268 ments are shown for the topography model in figure 5. The minimum period is an es-
 269 timation, and there is no sharp cut-off period for valid synthetics. Correlations become
 270 just more and more inaccurate for periods shorter than this estimate. From what we saw
 271 from simulations, they are usually sufficiently accurate only up to about 10 Hz from es-
 272 timated values, and this value does not only depend on the mesh size and density, but
 273 also on details of the seismic-source modeling.

274 Source distribution affects surface-waves amplitudes (Tsai & Moschetti, 2010), it
 275 influences correlograms and its knowledge is important to correctly interpret the data
 276 (Hanasoge et al., 2012; Basini et al., 2012). For cross-correlation simulations, the dis-
 277 tribution of noise sources in SPECFEM3D Cartesian is constrained to the surface, which
 278 is not a major drawback since the most relevant seismic sources in the NN band are ex-
 279 pected to be surface sources. Also, we defined the ensemble of seismic sources used for
 280 the cross-correlation simulation to have a minimum distance to the center of the model
 281 surface since we assume that these areas will be protected in the future, i.e., excluding

282 the presence of strong seismic sources inside the protected area. The radius of this area
 283 was also varied in our study to see the impact on seismic spectra and correlations. This
 284 also implies that the ET infrastructure must not introduce significant perturbations it-
 285 self, which requires a novel low-noise infrastructure design avoiding some of the errors
 286 made with current detector infrastructure.

287 5 Noise cross-correlation simulations

288 Ambient-noise seismology is of great relevance to high-resolution crustal imaging.
 289 Thanks to the unprecedented dense data coverage, it affords in regions of little seismic-
 290 ity (Basini et al., 2012). Cross-correlations between seismograms that recorded diffuse
 291 seismic wavefields created by stochastic wave excitation at the Earth’s surface at differ-
 292 ent seismographic stations show statistically significant signals to be present (Tromp et
 293 al., 2010). A common interpretation of noise cross-correlations is to relate them to a form
 294 of the Green’s function between two receivers (Lobkis & Weaver, 2001; Wapenaar et al.,
 295 2006; Fan & Snieder, 2009; Montagner et al., 2012). The method implemented in SPEC-
 296 FEM3D is best described in (Tromp et al., 2010), where it extends to the application of tomog-
 297 raphy and evaluating misfits between models and observations.

The solution for boundary problems of the elastodynamic equation can be expressed
 with the help of the Green’s tensor \mathbf{G}

$$\mathbf{s}(\mathbf{x}, t) = \int_{-\infty}^t \int_{\Omega} \mathbf{G}(\mathbf{x}, \mathbf{x}'; t - t') \cdot \mathbf{f}(\mathbf{x}', t') d^3\mathbf{x}' dt'. \quad (1)$$

The Green’s tensor satisfies the relationship (Aki & Richards, 2009; Dahlen et al., 1998)

$$\mathbf{G}(\mathbf{x}, \mathbf{x}'; t - t') = \mathbf{G}^T(\mathbf{x}', \mathbf{x}; t - t'). \quad (2)$$

In frequency domain, the solution can be expressed using the Fourier transform

$$\mathbf{s}(\mathbf{x}, \omega) = \int_{\Omega} \mathbf{G}(\mathbf{x}, \mathbf{x}'; \omega) \cdot \mathbf{f}(\mathbf{x}', \omega) d^3\mathbf{x}'. \quad (3)$$

298 In practice, one uses an ‘ensemble average’ of many cross-correlations, which we will re-
 299 fer to as the *ensemble cross-correlation*. One of the most important data-processing tech-
 300 niques in all of the ambient-noise seismology is ensemble averaging, allowing to reduce
 301 the effects of a set of scatterers and sources randomly distributed in time and space to
 302 those of a diffuse wavefield (Basini et al., 2013). Ensemble-averaged cross-correlations
 303 between synthetic seismograms at two geographically distinct locations on the free sur-
 304 face are determined under the assumption that noise is spatially uncorrelated but non-
 305 uniform. We focus our study on seismic surface measurements, despite the advantages
 306 of deeper seismometer installations (Mandic et al., 2018).

Let us consider the $\hat{\mathbf{v}}^\alpha$ component of the displacement at location \mathbf{x}^α , and the $\hat{\mathbf{v}}^\beta$
 component of the displacement at location \mathbf{x}^β :

$$s^\alpha(t) \equiv \hat{\mathbf{v}}^\alpha \cdot \mathbf{s}(\mathbf{x}^\alpha, t), \quad s^\beta(t) \equiv \hat{\mathbf{v}}^\beta \cdot \mathbf{s}(\mathbf{x}^\beta, t) \quad (4)$$

The cross-correlation between those two time-series is given by

$$C^{\alpha\beta}(t) = \int s^\alpha(t + \tau) s^\beta(\tau) d\tau \quad (5)$$

We assume that sources of the field are spatially uncorrelated, which implies

$$\langle f_j(\mathbf{x}', t') f_m(\mathbf{x}'', t'') \rangle = S_{jm}(\mathbf{x}', t' - t'') \delta(\mathbf{x}' - \mathbf{x}'') \quad (6)$$

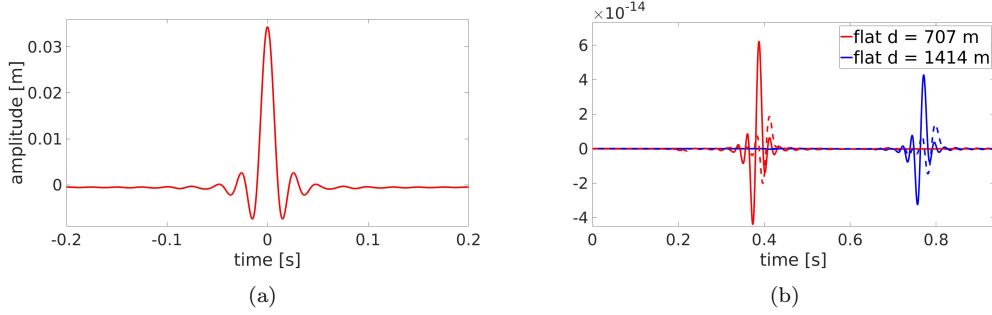


Figure 6: Source time function corresponding to the noise spectrum (a) and vertical displacement of generating wavefield for the flat and topography models at the locations with 707 m and 1414 m distance from the source (b). The dashed, colored curves in (b) mark with corresponding colors the vertical displacement of generating wavefield with topography.

307 where $\langle \cdot \rangle$ denotes an ensemble average (Woodard, 1997). S_{jm} describes the geographic
 308 and geometric properties and ω -dependence of the noise sources, it is non-zero only at
 309 the (surface) locations of the seismic sources.

Using Fourier transform, a representation in terms of the Green's tensor, and taking into consideration ensemble average and equation (2), the analytical expression for ensemble cross-correlation is:

$$\langle C^{\alpha\beta} \rangle (t) = \frac{1}{2\pi} \hat{v}_i^\alpha \hat{v}_\ell^\beta \iint S_{jm}(\mathbf{x}, \omega) G_{ji}(\mathbf{x}, \mathbf{x}^\alpha; \omega) G_{m\ell}^*(\mathbf{x}, \mathbf{x}^\beta; \omega) \exp(i\omega t) d^3\mathbf{x} d\omega. \quad (7)$$

One may notice that ensemble cross-correlations have the symmetry:

$$\langle C^{\alpha\beta} \rangle (t) = \langle C^{\beta\alpha} \rangle (-t). \quad (8)$$

310 The more detailed calculation can be found in (Tromp et al., 2010).

311 Our noise cross-correlation simulations require two steps. In the first step, one calculates a
 312 generating wavefield obtained by inserting a source-time function at the location of the first
 313 receiver. The source-time function of the generating wavefield is obtained using the spectrum
 314 of the ensemble-averaged noise, and it is narrowly concentrated around zero time. We use a
 315 source-time function shown in figure 6a representing a frequency-independent seismic spectrum
 316 in the interesting frequency range (1 – 30 Hz), since the absolute values of the seismic
 317 spectrum are not relevant for this paper. Generally, results in frequency domain can be
 318 rescaled using realistic / observed seismic spectra when needed. Then, the results of the
 319 generating wavefield are saved at each time step at locations where the actual noise sources
 320 are located, which in our simulation covers an area of the free surface. Displacement in the
 321 vertical direction of the generating wavefield for the flat and topography models at two
 322 locations with different distances from the source are shown in figure 6b.
 323

Next, in the second step, one uses this generating wavefield at the locations of the noise sources as sources of the ensemble forward wavefield associated with the first receiver. We assume that the excitation is along the vertical direction of the surface. In the case of vertical forces, more than two thirds of the total energy is radiated as Rayleigh waves (Woods, 1968). Regarding our application, at the surface, the relative amount of Rayleigh waves is even larger (Sanchez-Sesma & Campillo, 1991). It should also be noted that in our models, which basically represent a homogeneous halfspace, no other modes

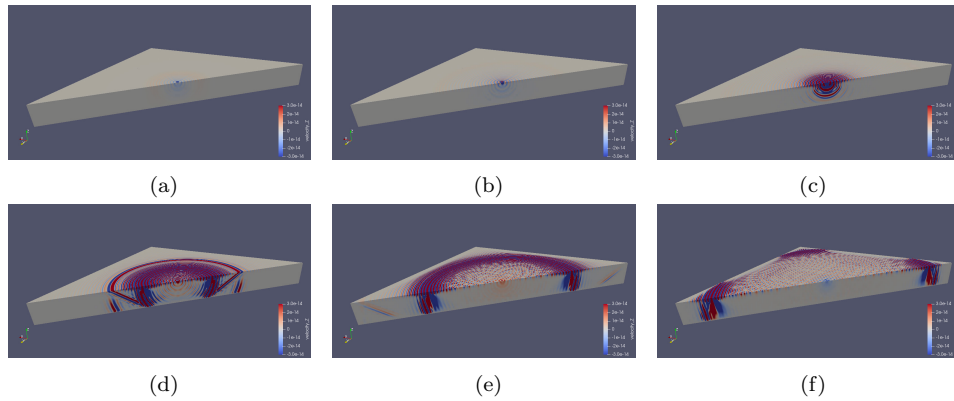


Figure 7: Propagation of seismic waves for the flat surface model using a source time function determined by the spectrum of the ensemble-averaged noise.

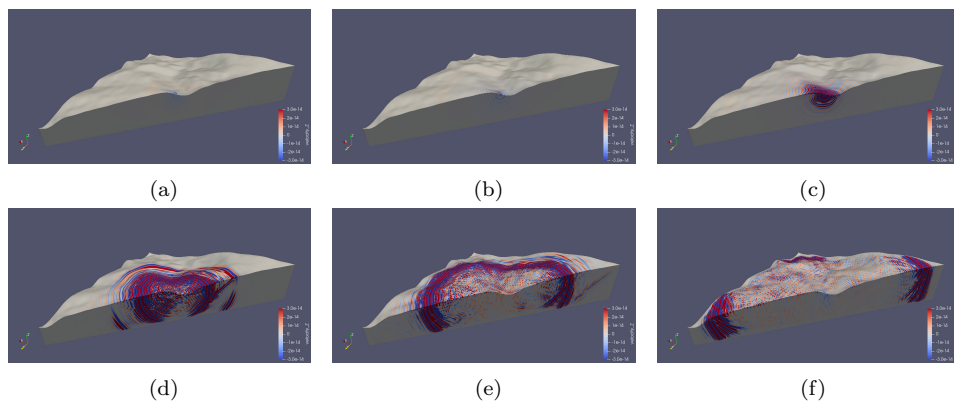


Figure 8: Propagation of seismic waves for the A3 topography model using a source time function determined by the spectrum of the ensemble-averaged noise.

of Rayleigh waves, apart from the fundamental Rayleigh mode, are possible. The source of the ensemble forward wavefield is just the time-reversed generating wavefield. The ensemble cross-correlation is equal to the $\hat{\mathbf{v}}^\alpha$ component of the ensemble forward wavefield Φ^β evaluated at location \mathbf{x}^α :

$$\langle C^{\alpha\beta} \rangle (t) = \hat{\mathbf{v}}^\alpha \cdot \Phi^\beta (\mathbf{x}^\alpha, t). \quad (9)$$

324 Having in mind equation (8), it is clear that knowing either Φ^α or Φ^β the ensemble cross-
 325 correlation can be calculated. More details can be found in (Tromp et al., 2010). A se-
 326 quence of snapshots resulting from a simulation of the wavefield with a source at the center
 327 of the model surface with the source time function as in figure 6a can be seen in fig-
 328 ure 7 for the flat model and in figure 8 for the A3 topography model.

329 6 Sensitivity kernels

330 Another step can be taken with noise cross-correlation simulations to obtain sensi-
 331 tivity kernels, which quantify the sensitivity of the cross-correlations to parameters of
 332 the ground medium such as mass density and seismic speeds. In addition to the gener-
 333 ating and ensemble forward wavefield described in section 5, the calculation of sensitiv-
 334 ity kernels requires another wavefield called ensemble adjoint wavefield. The sensitivity

335 kernel results from an interaction between the ensemble forward wavefield and the en-
 336 semble adjoint wavefield. It is then possible to estimate sensitivity kernels without re-
 337 quiring computationally expensive ensemble averages as done in practice when analyz-
 338 ing seismic data (substituting ensemble averages by temporal averages). As a technical
 339 note, the calculation of sensitivity kernels with SPECFEM3D does not currently sup-
 340 port C-PML. We used Clayton-Enquist boundary conditions for these simulations.

341 In seismology, sensitivity kernels are very important for tomographic inversion and
 342 can be used to improve Earth and source models. They illuminate those parts of mod-
 343 els that are inaccurate. In other words, using observed correlations and making simu-
 344 lations of synthetic correlations, one uses the cross-correlation misfit to iteratively im-
 345 prove the model. More about ensemble adjoint wavefield and sensitivity kernels can be
 346 found in (Liu & Tromp, 2006; Tromp et al., 2005; Tromp et al., 2008; Tromp et al., 2010;
 347 Peter et al., 2011). Sensitivity kernels are not of direct relevance to our work, but they
 348 give additional information whether the model size is sufficiently large for the simula-
 349 tion of correlations, in which case sensitivity kernels should be small towards the bound-
 350 aries of the model. For the future, they can guide the development of more sophisticated
 351 models with inhomogeneous geology.

352 The theoretical work in (Tromp et al., 2010) shows how adjoint techniques (e.g. (Tromp
 353 et al., 2005; Peter et al., 2007)) can be applied to ambient-noise seismology taking into
 354 account the non-uniform distribution of noise sources. The ensemble adjoint wavefield
 355 is produced by a source located at the second receiver whose time function depends on
 356 the misfit between simulated and observed correlations. There are various possibilities
 357 to evaluate cross-correlation misfits. The method chosen in SPECFEM3D is based on
 358 the misfit of cross-correlation delay times. The cross-correlation delay time would for ex-
 359 ample be responsible for a complex phase of cross-spectral densities between sensors. Since
 360 we are only interested in the sensitivity kernel and not in the actual inference of ground
 361 properties using seismic observations, an arbitrary misfit of $\Delta T = 1$ s is chosen (Tromp
 362 et al., 2010).

363 The ensemble adjoint source corresponding to a delay-time misfit involves the first
 364 time derivative of the simulated ensemble cross-correlation $\langle \dot{C}^{\alpha\beta} \rangle$. As will be shown sub-
 365 sequently, ensemble cross-correlations are dominated by Rayleigh surface waves, whose
 366 main sensitivity is to shear-wave speed (often given the symbol β). So here, we focus on
 367 beta kernels. The beta kernel is a volumetric field representing the gradient of the mis-
 368 fit function with respect to S-wave speed.

369 The beta kernel is shown in figure 9 for the flat (top) and for the A3 topography
 370 model (bottom). One can see that cross-correlations are most sensitive to properties of
 371 the ground close to and between the two receivers and close to the surface. Note that
 372 the kernel is asymmetric with respect to an exchange of receivers. This asymmetry comes
 373 from the fact that kernels are defined for two branches, the so-called positive and neg-
 374 ative branch (the positive branch being shown). The positive branch describes cross-correlations
 375 whose time delays are consistent with waves reaching the second receiver before the first.

376 If we interpreted the 1 s time delay as an observed misfit, then the plots in figure
 377 9 would tell us that the S-wave speed in the region between the two receivers, since the
 378 kernel is negative here, would have to be decreased to reduce the time-delay misfit be-
 379 tween observation and model. The sign of the kernel would be inverted in the negative
 380 branch since the model would have to be corrected to increase a negative time delay.

381 7 Results

382 Einstein Telescope targets GW observations down to a few Hz (Punturo et al., 2010),
 383 which means that seismic NN will play an important role for instrument design. The de-
 384 tector will be hosted in an underground infrastructure, which creates a low-noise envi-

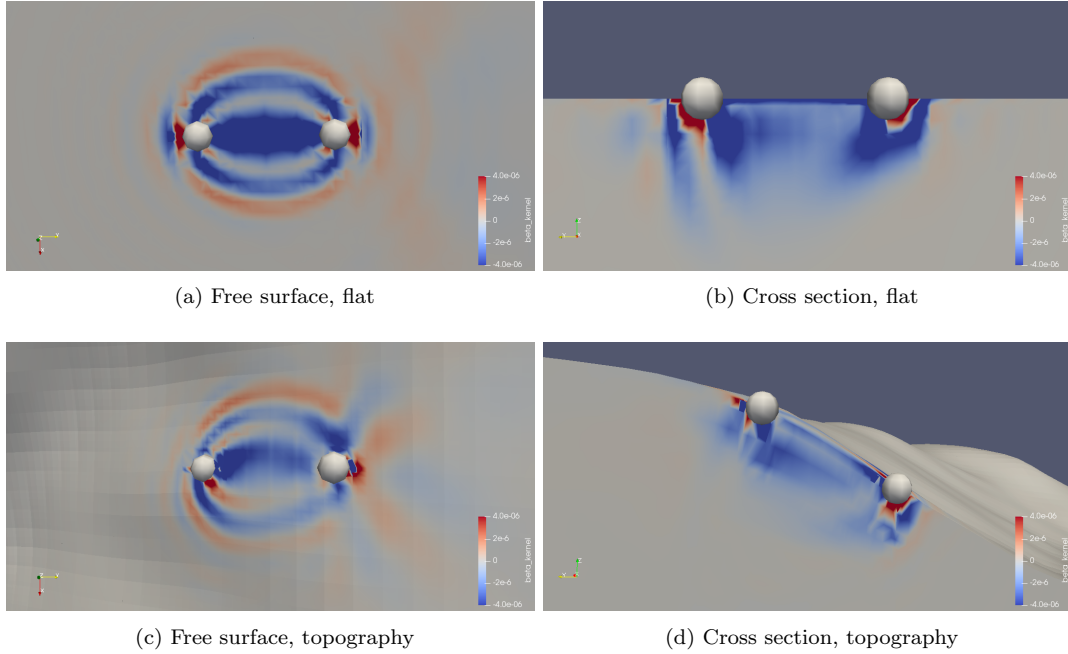


Figure 9: Beta kernel for flat (top row) and topography surface model (bottom row). White spheres represent receivers at a distance of 130 m from each other.

385 ronment providing an essential reduction of NN. Detector infrastructure including pumps
 386 and ventilation must not disturb the underground environment or be at a safe distance
 387 to the test masses. Further mitigation of NN can be achieved by noise cancellation using
 388 an extensive monitoring system of the ambient seismic field (Harms, 2019). The idea
 389 is to pass seismic data through a filter such that its output can be understood as a co-
 390 herent estimate of seismic NN and be subtracted from the GW data (Cella, 2000). These
 391 filters can take the form of Wiener filters calculated from the correlations between seis-
 392 mometers and the GW detector. The most challenging aspect of this technology is to
 393 determine the locations of a given number of sensors that optimize the cancellation per-
 394 formance (M. Coughlin et al., 2016; Badaracco & Harms, 2019).

395 Rayleigh waves are predicted to give the dominant contribution to NN in surface
 396 detectors (M. Coughlin et al., 2016; Harms et al., 2020) and even underground detec-
 397 tors can still be limited by gravitational noise from Rayleigh waves depending on the de-
 398 tector depth (Badaracco & Harms, 2019). The Rayleigh field produces surface displace-
 399 ment and density perturbations beneath the surface at the same time (Hughes & Thorne,
 400 1998; Beccaria et al., 1998), which leads to gravity perturbations. Even if we do not know
 401 the wave composition of a seismic field at a site, it is still reasonable in many cases to
 402 assume that Rayleigh waves dominate the normal surface displacement at frequencies
 403 in the range 1 Hz – 20 Hz produced by surface or near-surface seismic sources (Mooney,
 404 1976; Bonnefoy-Claudet et al., 2006). Only at exceptionally quiet (necessarily remote)
 405 surface sites or underground sites, body-wave content is expected to be significant or do-
 406 minant in this band (however, mode content can change significantly with time if due to
 407 natural sources (M. Coughlin et al., 2019)).

408 In the following, we present results of our analyses of spatial correlations in an ambi-
 409 ent seismic field simulated with SPECFEM3D, and we predict the correlation between
 410 surface seismometers and the gravity perturbation experienced by an underground test

411 mass, which is the crucial information for the optimization of surface arrays for NN can-
 412 cellation. As already explained, our analyses are constrained by the computational re-
 413 sources that were available to us. One consequence is that it was not possible to run a
 414 simulation with a test-mass depth greater than 100 m (while 200 m – 300 m is the envi-
 415 sioned depth of ET test masses), since this would have required a dense set of receivers
 416 distributed over a much larger surface area. We learn from these results how topogra-
 417 phy impacts correlations, which we expect to be the main site effect on seismic corre-
 418 lations and seismic gravitational noise.

419 7.1 Seismic scattering

420 The effect of scattering of seismic waves from surface topography on seismic cor-
 421 relation and gravity perturbations of test masses needs to be quantified using the meth-
 422 ods outlined in section 5. As mentioned earlier, because of the way we choose to excite
 423 seismic waves in this analysis, the ensemble forward field is mainly composed of Rayleigh
 424 surface waves. For flat, free surfaces, Rayleigh waves, once decoupled from the near field
 425 of the seismic sources, propagate without conversion into other seismic modes.

426 The scattering by topography depends on the size of elevation changes, area of con-
 427 tact, and the length scale of the irregularity. It also depends significantly on incident an-
 428 gle and type of seismic waves propagating through the area. Amplitudes of scattered waves
 429 should increase linearly with the size of elevation changes for small obstacles according
 430 to perturbation theory based on the first-order Born approximation (Gilbert & Knopoff,
 431 1960). Born approximation breaks down for steeper slopes (steeper than approximately
 432 30°) and higher elevations of topography (depending on wavelength of seismic waves and
 433 horizontal dimension of topography), for which there is strong amplification of scattered
 434 waves (Snieder, 1986; Hudson et al., 1973). Therefore, the scattering should be much re-
 435 duced in the case of irregularities with gentle curvature when compared with irregular-
 436 ities (mountains) with abrupt discontinuities in curvature (bluff topography) (Gilbert
 437 & Knopoff, 1960). An important point is that the incident wave is essentially "blind"
 438 to features that are much smaller than a wavelength (Otto, 1977). Scattering always be-
 439 comes weaker at smaller frequencies if all other parameters are kept constant, but gen-
 440 erally, there is no simple frequency scaling valid for the entire wavenumber space. Scat-
 441 tering coefficients in wavenumber space are mainly proportional to the topographic spec-
 442 trum (M. Coughlin & Harms, 2012). The maximum scattering is generally present when
 443 seismic wavenumbers match the wavenumbers of the topographic spectrum (J. Hudson
 444 & Knopoff, 1967).

445 In our ensemble forward wavefield, there is also body-wave content. So, it is inter-
 446 esting to see what happens with body waves during scattering in addition to the dom-
 447 inant Rayleigh-wave field. In the case of incident S-waves, if the dominant horizontal length
 448 scales of the surface spectrum are small compared with the length of incident waves, the
 449 amplitudes of some of the scattered waves decrease exponentially with depth similar to
 450 Rayleigh waves. A periodic surface characterized by short horizontal length scales traps
 451 more of the incident energy than one characterized by longer length scales, but the amount
 452 of trapped energy also depends on the associated amplitudes of the topographic spec-
 453 trum. This trapped energy feeds into the surface waves (Abubakar, 1962).

454 For the incident P-waves, scattered waves are mostly Rayleigh waves accompanied
 455 by a weaker (horizontal) P-wave (Bard, 1982). The amplitude ratio of scattered Rayleigh
 456 to incident longitudinal wave depends mostly on angle of incidence and horizontal and
 457 vertical dimension of the corrugation. For example, for normally incident longitudinal
 458 waves, with Rayleigh wavelength equal to the width of corrugation, amplitude ratio grows
 459 linearly with ratio of horizontal and vertical dimensions of the corrugation. Already at
 460 ratios of horizontal and vertical dimensions less than one, scattered Rayleigh wave has
 461 surface amplitude that is greater than that of the incident longitudinal wave alone (Hudson

et al., 1973). In conclusion, a significant percentage of bulk waves scatter into Rayleigh waves and additionally that scattering is driven by high-wavenumber components of the surface topography, which typically have weaker amplitudes.

For incident Rayleigh waves, which is the most interesting case for us, scattering effects were investigated in (Maradudin & Mills, 1976). The main conclusion that one may draw from there is that the predominant contribution from the roughness-induced scattering of the incident Rayleigh wave is into other Rayleigh waves. At low frequencies, the ratio between scattered Rayleigh and bulk waves is about 10, and it grows as the frequency increases. So Rayleigh wave/Rayleigh wave scattering contribution is about an order of magnitude larger than the bulk wave contributions. However, details depend on the topography.

Scattering especially from Rayleigh waves into Rayleigh waves is a very efficient scattering channel, but since it does not cause a change in wave type, its impact on NN cancellation can easily be modeled. Still, it is found that topographic scattering might be relevant to NN subtraction in regions with rough topography (M. Coughlin & Harms, 2012). Fields of scattered waves do not generally permit a unique correspondence between frequency and wavelength, since at each frequency, the wavenumber spectrum of the scattered field is typically continuous. This is the main challenge for the design of a NN cancellation system in seismic fields with significant contributions from scattered waves. We need to mention that also scattering from underground caverns of the Einstein Telescope would significantly modify the seismic field in the vicinity of the cavern, but the impact on NN remains small as long as the caverns are much smaller than the seismic wavelengths in the relevant frequency range (Harms, 2019).

As a first characterization of topographic scattering, we calculate the ratio of power spectral densities at the center of our models with and without topography. The ratio is shown in figure 10 between 1 Hz and 30 Hz for three different minimal distances of seismic sources to the center point. The plot shows that higher frequencies are more scattered out with respect to lower frequencies by topography. In other words, topography acts as a low-pass for Rayleigh waves protecting a point to some extent from the influence of distant seismic sources. At the A3 vertex of the Einstein Telescope, topographic protection is provided down to about 4 Hz. As can be seen, the ratio depends weakly on the minimal distance of seismic sources, which can be explained by the contribution of increasingly large topographic scales to the scattering coefficients. Of course, the absolute value of power spectral density reduces significantly when sources are more distant.

7.2 Seismic coherence

The SPECFEM3D simulation of seismic correlations yields a time-domain correlation $C_{ij}(\tau)$ between two receivers. For our analysis, we need the Fourier transform,

$$S_{ij}(f) = \int_{-\infty}^{\infty} d\tau C_{ij}(\tau) e^{i2\pi f\tau}, \quad (10)$$

which, according to the Wiener-Khinchin theorem, is the cross power-spectral density (CPSD) between the two sensors. The CPSD can be normalized so that its absolute value lies between 0 and 1, a quantity called *coherence*:

$$c_{ij}(f) = \frac{S_{ij}(f)}{\sqrt{S_i(f)S_j(f)}}. \quad (11)$$

Figure 11 summarizes four analyses of seismic coherence with SPECFEM3D. In plot (a), we show the absolute value of coherence for the flat-surface and A3-topography models with varying minimal distances of seismic sources of the ambient field. While the coherence is significantly different between the two models, it only depends weakly on the

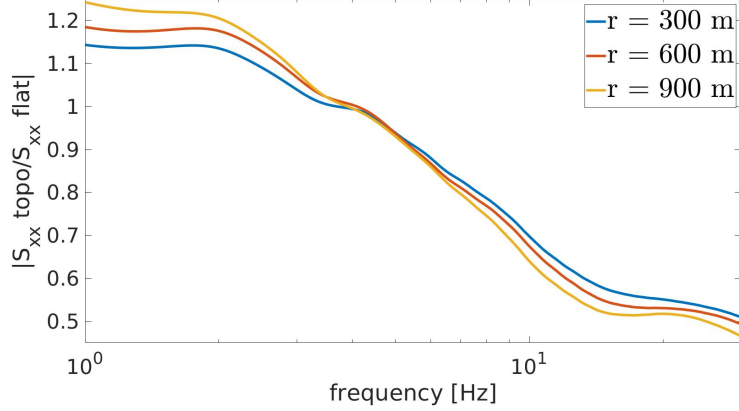


Figure 10: Ratio of seismic spectral densities at the center of topographic (A3 vertex) and flat models for different values of the minimal distance of seismic sources.

minimal distance of sources. The plot also contains an analytical prediction of coherence for the flat-surface, isotropic Rayleigh-wave field, where the coherence is given by a Bessel function

$$c_{ij}(f) = J_0(2\pi f|\vec{r}_j - \vec{r}_i|/c) \quad (12)$$

with a Rayleigh-wave speed of $c = 1840$ m/s. In this simple case, the coherence is real-valued, but it is generally a complex quantity. The distance between the two receivers is 130 m.

Plot (b) displays the absolute value of coherence for varying distance between the two receivers. Again, the coherence obtained from the A3-topographic model is qualitatively different from the flat-surface coherence for all distances between receivers. With the A3-topographic model, $|c_{ij}(f)|$ does not vanish at any frequency, which is likely due to a mixed wave content with Rayleigh waves and scattered waves of different wavelengths.

In plot (c), we verify that the size of the standard finite-element model ($3 \text{ km} \times 3 \text{ km}$) was not chosen too small for analyses in this paper, i.e., that coherence changes weakly when increasing model size. While some change in coherence can be observed, it is minor especially in the frequency band of interest 3 Hz – 10 Hz, where NN might limit the sensitivity of Einstein Telescope.

Finally, in plot (d), $|c_{ij}(f)|$ is shown as a function of distance at frequency 5 Hz. The aforementioned qualitative difference between the flat-surface and A3-topographic models can be seen again. The flat-surface model closely follows the analytical model of an isotropic, flat-surface Rayleigh-wave field.

7.3 Gravity-displacement correlation

It is possible to express the gravity perturbation produced by a seismic field in terms of an integral over seismic correlations (Harms, 2019). It is possible to separate contributions from compression and decompression of the ground medium by seismic waves and from surface displacement. Surface displacement is typically much stronger than underground displacement due to the presence of surface waves such as Rayleigh waves. One of the reasons why Einstein Telescope is proposed as underground infrastructure is to avoid the relatively strong gravitational noise from surface displacement (Amann et al., 2020).

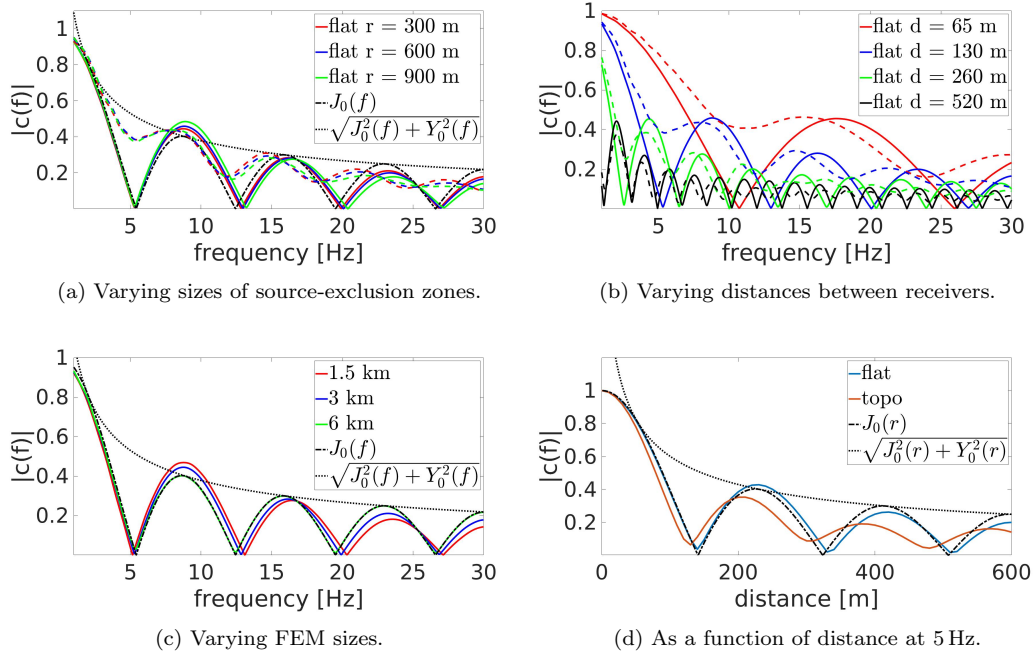


Figure 11: Plots of seismic coherence calculated by SPEC3D. The dashed, colored curves in (a) and (b) mark with corresponding colors the coherence with topography.

As a consequence, and as a first step, we attempt to model the gravitational coupling between seismic surface fields and underground gravitational perturbations. The equation to be used takes the form of a surface integral (Harms, 2019)

$$C(\delta a_{\text{arm}}(\mathbf{r}_0), \xi_z(\mathbf{r}); f) = G\rho_0 \int d^2\mathbf{r}' C(\xi_n(\mathbf{r}'), \xi_z(\mathbf{r}); f) \frac{(\mathbf{r}' - \mathbf{r}_0) \cdot \mathbf{e}_{\text{arm}}}{|\mathbf{r}' - \mathbf{r}_0|^3}, \quad (13)$$

524 which is the CPSD between vertical seismic displacement ξ_z monitored at \mathbf{r} and hori-
 525 zontal gravitational acceleration δa_{arm} at the location \mathbf{r}_0 of an underground test mass.
 526 Here, G is Newton's gravitational constant, ρ_0 is the mass density of a homogeneous ground,
 527 and \mathbf{e}_{arm} is the unit vector pointing along the detector arm of Einstein Telescope. The
 528 integral contains the CPSD between vertical and normal surface displacement provided
 529 by SPEC3D simulations. We focus on normal surface displacement typically asso-
 530 ciated with Rayleigh waves since lateral surface displacement does not produce gravity
 531 perturbations. This also explains why in this study we are not interested in contribu-
 532 tions from Love waves, which can only generate gravity perturbations by displacement
 533 of underground cavern walls of the detector. In any case, our homogeneous model does
 534 not support the simulation of Love waves. Since a homogeneous medium is simulated
 535 here, Love waves do not play a role, but it is still convenient for practical reasons (when
 536 comparing with other work or seismic observations) to focus on vertical displacement.

537 The seismic CPSD $C(\xi_n(\mathbf{r}' = \mathbf{0}), \xi_z(\mathbf{r}); f)$ for the A3-topographic model is shown
 538 in plot (a) of figure 12. It only represents a small subset of all seismic correlations re-
 539 quired for equation (13). The result can be compared with the seismic CPSD in the case
 540 of a flat-surface, isotropic Rayleigh wave field shown in plot (b). Topography has a sig-
 541 nificant impact on seismic correlations, but the pattern of concentric rings is approxi-
 542 mately preserved. The third plot shows the variation of power spectral densities of ver-
 543 tical surface displacement. Again, topography leaves a clear imprint on the seismic field
 544 in the form of an inhomogeneity.

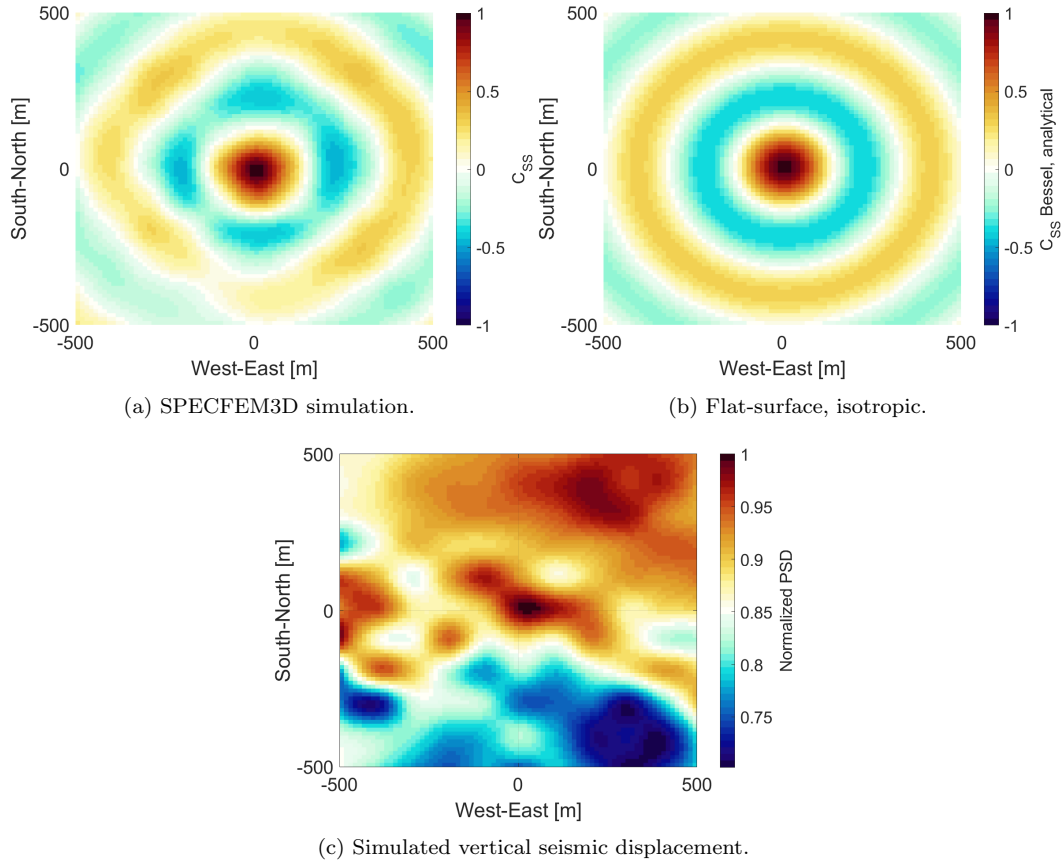


Figure 12: Normalized correlations (a) and spectral densities (c) calculated for an ambient field with SPECFEM3D at 5 Hz. The ideal (normalized) seismic correlations in the case of a flat surface and isotropic field is shown in (b).

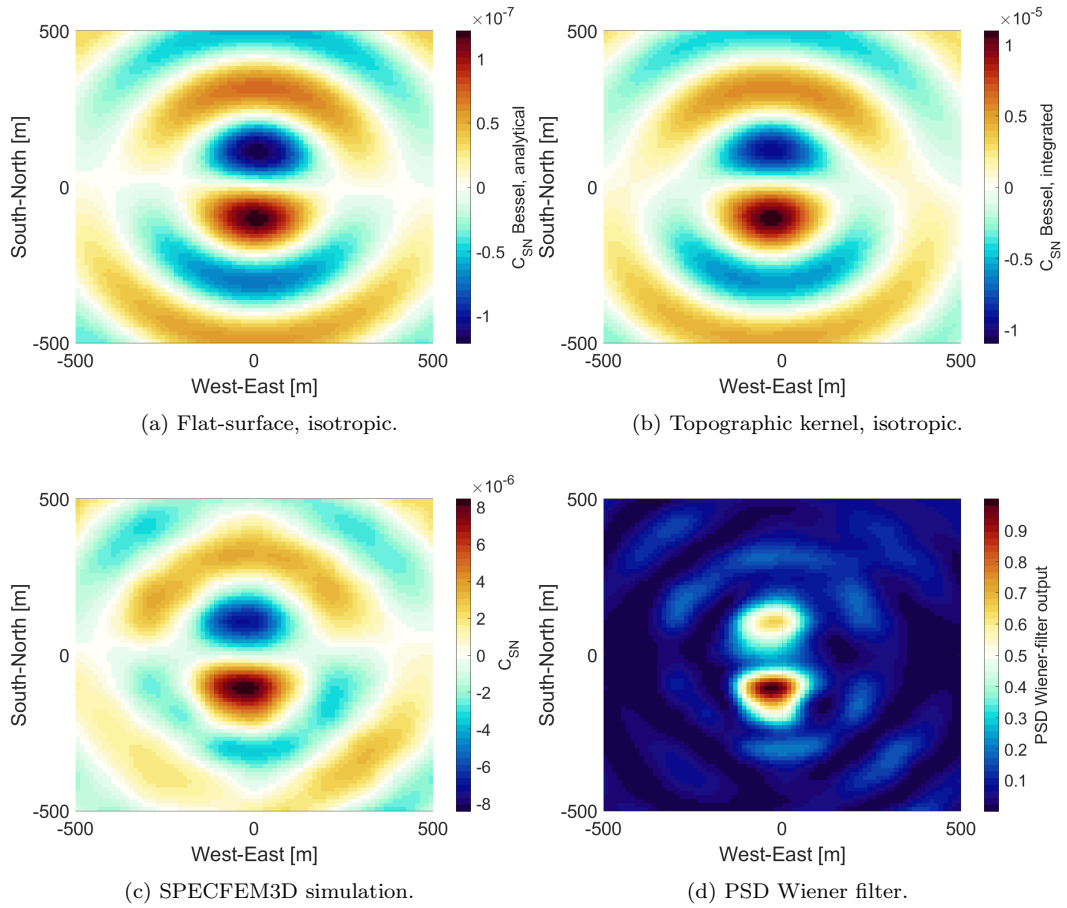


Figure 13: Seismic-gravitational correlations of an ambient field at 5 Hz (a) – (c) in arbitrary, but consistent units. The normalized PSD of the Wiener-filter output is shown in (d). The test mass is located 100 m underground. The direction of gravity acceleration is along the A3 – A1 detector arm.

Equation (13) can be solved analytically in the case of a flat-surface, isotropic Rayleigh field, which yields (Harms, 2019):

$$C(\delta a_{\text{arm}}(\mathbf{0}), \xi_z(\mathbf{r}); f) = 2\pi G\rho_0 S(\xi_z; f) e^{-hk(f)} \cos(\phi) J_1(k(f)r), \quad (14)$$

545 with $\mathbf{r} = (r \cos(\phi), r \sin(\phi), h)$, ϕ being the angle between detector arm and the hori-
 546 zontal projection of \mathbf{r} , and $k(f)$ is the wavenumber of plane Rayleigh waves. According
 547 to this model, the CPSD between vertical displacement and gravity perturbation van-
 548 ishes for $\mathbf{r} = \mathbf{0}$. It is shown in plot (a) of figure 13. Instead, plot (b) is calculated by
 549 inserting the isotropic, flat-surface correlation of equation (12) into equation (13), but
 550 with a kernel that depends on topography. This shows that the kernel has an important
 551 impact on the seismic-gravitational CPSD, e.g., the nodal line along the south-north di-
 552 rection seen in plot (a) is not present in plot (b). Finally, the seismic-gravitational CPSD
 553 calculated with the seismic CPSD from SPEC-FEM3D and topographic kernel in equa-
 554 tion (13) is shown in plot (c).

The result in plot (d) tells us where a single seismometer should be placed to ob-
 tain the best reduction of NN by coherent cancellation with a Wiener filter. The plot-
 ted quantity is

$$S(w; f) = |C(\delta a_{\text{arm}}(\mathbf{r}_0), \xi_z(\mathbf{r}); f)|^2 / C(\xi_z(\mathbf{r}), \xi_z(\mathbf{r}); f), \quad (15)$$

555 which is the power spectral density of the output of the Wiener filter (Cella, 2000; Harms,
 556 2019). The higher it is, the more NN the Wiener filter is able to cancel in the data of
 557 the Einstein Telescope. This optimal placement of a seismometer is at (-38 m, -113 m).
 558 The problem gets significantly more complicated if one wants to deploy multiple seis-
 559 mometers since the placement of sensors also depends on their mutual CPSDs (Badaracco
 560 & Harms, 2019). Nonetheless, the quantities required for such a multi-sensor optimiza-
 561 tion are provided by SPEC-FEM3D. They need to be used in numerical optimization rou-
 562 tines. What we in fact propose is to use the correlation results from numerical analy-
 563 sis as presented in this paper to define priors for a Gaussian Process Regression, which
 564 then combines priors and observed seismic correlations for a Bayesian inference of seis-
 565 mic correlations everywhere in the medium, which forms the basis of the optimization
 566 algorithm (Badaracco et al., 2020).

567 8 Conclusion

568 In this paper, we presented synthetic seismic and gravitoelastic correlations between
 569 seismometers and a suspended underground test mass as part of the next-generation, gravita-
 570 tional-wave detector Einstein Telescope. The synthetics were calculated with the spectral-element
 571 SPEC-FEM3D Cartesian software. The main analysis was based on a topographic model
 572 centered at one of the vertices (A3) at a candidate site in Sardinia of the Einstein Tele-
 573 scope.

574 We found that A3 topography has generally a significant impact on seismic and grav-
 575 itoelastic correlations. Specifically, calculations showed that Sardinian topography at ver-
 576 tex A3 scatters out energy from Rayleigh waves above 4 Hz providing protection from
 577 the influence of distant seismic sources. As expected, symmetries of the field of gravi-
 578 toelastic correlations are broken by topography leading to unique solutions of optimal
 579 seismometer placement for gravity-noise cancellation.

580 The results are a powerful demonstration of SPEC-FEM3D's capability to model
 581 correlations in ambient seismic fields for the purpose of designing noise-cancellation sys-
 582 tems using seismometer arrays. We proposed to use the numerical results to define pri-
 583 ors of a Gaussian Process Regression, which includes seismic observations to infer gravi-
 584 toelastic correlations throughout the entire ground medium. This is a crucial step to
 585 calculate optimal array configurations for gravity-noise cancellation, which we expect to

586 require several tens to hundreds of seismometers deployed in boreholes around 12 of the
587 test masses of the Einstein Telescope.

588 Since this work only addressed gravity perturbations from seismic surface displace-
589 ment, an important future task is to extend the analysis to gravity perturbations result-
590 ing from (de)compression of rock by seismic waves, and from displacement of underground
591 cavern walls. In addition, geological inhomogeneities may be significant, which means
592 that they should also be included in future modeling. Current understanding of geology
593 near the three vertex locations can be improved by drill-core and geoseismic studies, which
594 would help to build a more accurate model and to improve simulation results.

595 Acknowledgments

596 To prepare the topography data one can get SRTM Digital Elevation Data for a region
597 of interest at: <http://srtm.csi.cgiar.org>. Besides, this is a modeling and simulation pa-
598 per. There is no data necessary to understand, evaluate, or replicate our results. It is
599 all based on creating a model and running the simulations on it, which anyone can re-
600 peat in principle with the information in the paper. SPEC3D is maintained by the
601 Computational Infrastructure for Geodynamics (<http://geodynamics.org>), which is funded
602 by the National Science Foundation under awards EAR-0949446 and EAR-1550901. The
603 work was supported by the PRIN project “Characterization of the Sos Enattos mine in
604 Sardinia as the site for the Einstein Telescope GW observatory”. We thank the Sardinia
605 site-study team for useful discussions and suggestions for this manuscript. We acknowl-
606 edge the usage of the high-performance cluster at CNAF, the central computing facil-
607 ity of INFN at Bologna. We are grateful for the continuous support we received from
608 its staff.

609 References

- 610 Abbott, B. P., Abbott, R., Abbott, T. D., Abernathy, M. R., Acernese, F., Ackley,
611 K., ... Zweizig, J. (2016, March). GW150914: The Advanced LIGO Detectors
612 in the Era of First Discoveries. *Physical Review Letters*, 116, 131103. Re-
613 trieved from <http://link.aps.org/doi/10.1103/PhysRevLett.116.131103>
614 doi: 10.1103/PhysRevLett.116.131103
- 615 Abubakar, I. (1962, January). Scattering of plane elastic waves at rough sur-
616 faces. I. *Mathematical Proceedings of the Cambridge Philosophical So-*
617 *ciety*, 58, 136–157. Retrieved from [http://journals.cambridge.org/](http://journals.cambridge.org/article\S030500410003629X)
618 [article\S030500410003629X](http://journals.cambridge.org/article\S030500410003629X) doi: 10.1017/S030500410003629X
- 619 Abubakar, I. (1963, January). Scattering of plane elastic waves at rough surfaces.
620 ii. *Mathematical Proceedings of the Cambridge Philosophical Society*, 59, 231 –
621 248. doi: 10.1017/S0305004100002176
- 622 Acernese, F., Agathos, M., Agatsuma, K., Aisa, D., Allemandou, N., Allocca, A.,
623 ... others (2015). Advanced Virgo: a second-generation interferometric
624 gravitational wave detector. *Classical and Quantum Gravity*, 32(2), 024001.
625 Retrieved from <http://stacks.iop.org/0264-9381/32/i=2/a=024001> doi:
626 10.1088/0264-9381/32/2/024001
- 627 Acernese, F., Antonucci, F., Aoudia, S., Arun, K., Astone, P., Ballardin, G., ...
628 Yvert, M. (2010). Measurements of Superattenuator seismic isolation by
629 Virgo interferometer. *Astroparticle Physics*, 33(3), 182 - 189. Retrieved from
630 <http://www.sciencedirect.com/science/article/pii/S0927650510000253>
631 doi: <http://dx.doi.org/10.1016/j.astropartphys.2010.01.006>
- 632 Adhikari, R. X., Arai, K., Brooks, A. F., Wipf, C., Aguiar, O., Altin, P., ...
633 Zhao, C. (2020, jul). A cryogenic silicon interferometer for gravitational-
634 wave detection. *Classical and Quantum Gravity*, 37(16), 165003. Re-
635 trieved from <https://doi.org/10.1088/1361-6382/ab9143> doi:
636 10.1088/1361-6382/ab9143

- 637 Aki, K., & Richards, P. G. (2009). *Quantitative Seismology, 2nd edition*. University
638 Science Books.
- 639 Akutsu, T., et al. (2019). KAGRA: 2.5 Generation Interferometric Gravitational
640 Wave Detector. *Nature Astronomy*, *3*(1), 35-40. doi: 10.1038/s41550-018-0658
641 -y
- 642 Amann, F., Bonsignorio, F., Bulik, T., Bulten, H. J., Cuccuru, S., Dassargues, A.,
643 ... Vasuth, M. (2020, March). Site-selection criteria for the Einstein Tele-
644 scope. *arXiv e-prints*, arXiv:2003.03434.
- 645 Badaracco, F., & Harms, J. (2019, June). Optimization of seismometer arrays
646 for the cancellation of Newtonian noise from seismic body waves. *Classical
647 and Quantum Gravity*, *36*(14), 145006. Retrieved from [https://doi.org/
648 10.1088/1361-6382/ab28c1](https://doi.org/10.1088/1361-6382/ab28c1) doi: 10.1088/1361-6382/ab28c1
- 649 Badaracco, F., Harms, J., Bertolini, A., Bulik, T., Fiori, I., Idzkowski, B., ...
650 Suchinski, M. (2020). Machine learning for gravitational-wave detection:
651 surrogate Wiener filtering for the prediction and optimized cancellation of
652 Newtonian noise at Virgo. *Classical and Quantum Gravity*. Retrieved from
653 <http://iopscience.iop.org/10.1088/1361-6382/abab64>
- 654 Bard, P.-Y. (1982, December). Diffracted waves and displacement field over two-
655 dimensional elevated topographies. *Geophysical Journal of the Royal Astro-
656 nomical Society*, *71*(3), 731-760. doi: 10.1111/j.1365-246X.1982.tb02795.x
- 657 Barsotti, L., Harms, J., & Schnabel, R. (2019, January). Squeezed vacuum states
658 of light for gravitational wave detectors. *Reports on Progress in Physics*, *82*(1),
659 016905. doi: 10.1088/1361-6633/aab906
- 660 Basini, P., Liu, Q., & Tape, C. (2012, December). Ambient-noise Tomography of
661 the Southern California Lithosphere. In *Agu fall meeting abstracts* (Vol. 2012,
662 p. S41A-2415).
- 663 Basini, P., Nissen-Meyer, T., Boschi, L., Casarotti, E., Verbeke, J., Schenk, O., &
664 Giardini, D. (2013, May). The influence of nonuniform ambient noise on
665 crustal tomography in Europe. *Geochemistry, Geophysics, Geosystems*, *14*(5),
666 1471-1492. doi: 10.1002/ggge.20081
- 667 Beccaria, M., Bernardini, M., Braccini, S., Bradaschia, C., Bozzi, A., Casciano, C.,
668 ... Zhang, Z. (1998). Relevance of Newtonian seismic noise for the VIRGO
669 interferometer sensitivity. *Classical and Quantum Gravity*, *15*(11), 3339.
670 Retrieved from <http://stacks.iop.org/0264-9381/15/i=11/a=004>
- 671 Beker, M., Cella, G., DeSalvo, R., Doets, M., Grote, H., Harms, J., ... van Leeuwen,
672 C. (2011). Improving the sensitivity of future GW observatories in the 1
673 - 10Hz band: Newtonian and seismic noise. *General Relativity and Grav-
674 itation*, *43*(2), 623-656. Retrieved from [http://dx.doi.org/10.1007/
675 s10714-010-1011-7](http://dx.doi.org/10.1007/s10714-010-1011-7) doi: 10.1007/s10714-010-1011-7
- 676 Beker, M. G., van den Brand, J. F. J., Hennes, E., & Rabeling, D. S. (2012).
677 Newtonian noise and ambient ground motion for gravitational wave detec-
678 tors. *Journal of Physics: Conference Series*, *363*(1), 012004. Retrieved from
679 <http://stacks.iop.org/1742-6596/363/i=1/a=012004>
- 680 Beker, M. G., van den Brand, J. F. J., & Rabeling, D. S. (2015). Subterranean
681 ground motion studies for the Einstein Telescope. *Classical and Quantum
682 Gravity*, *32*(2), 025002. Retrieved from [http://stacks.iop.org/0264-9381/
683 32/i=2/a=025002](http://stacks.iop.org/0264-9381/32/i=2/a=025002)
- 684 Blacker, T., Quadros, R. W., Owen, S. J., Staten, M. L., Hanks, B., Clark, B., ...
685 Ressler, P. (2019). *Trelis v16.5 [software]*.
- 686 Bonnefoy-Claudet, S., Cotton, F., & Bard, P.-Y. (2006). The nature of
687 noise wavefield and its applications for site effects studies: A literature
688 review. *Earth-Science Reviews*, *79*(3-4), 205 - 227. Retrieved from
689 <http://www.sciencedirect.com/science/article/pii/S0012825206001012>
690 doi: <http://dx.doi.org/10.1016/j.earscirev.2006.07.004>
- 691 Cella, G. (2000). Off-Line Subtraction of Seismic Newtonian Noise. In

- 692 B. Casciario, D. Fortunato, M. Francaviglia, & A. Masiello (Eds.), *Recent*
693 *developments in general relativity* (p. 495-503). Springer Milan. Re-
694 trieved from http://dx.doi.org/10.1007/978-88-470-2113-6_44 doi:
695 10.1007/978-88-470-2113-6_44
- 696 Chan, M. L., Messenger, C., Heng, I. S., & Hendry, M. (2018, June). Binary neutron
697 star mergers and third generation detectors: Localization and early warning.
698 *Physical Review D*, *97*, 123014. Retrieved from [https://link.aps.org/doi/](https://link.aps.org/doi/10.1103/PhysRevD.97.123014)
699 [10.1103/PhysRevD.97.123014](https://link.aps.org/doi/10.1103/PhysRevD.97.123014) doi: 10.1103/PhysRevD.97.123014
- 700 Coughlin, M., & Harms, J. (2012). Seismic topographic scattering in the context of
701 GW detector site selection. *Classical and Quantum Gravity*, *29*, 075004. Re-
702 trieved from <http://stacks.iop.org/0264-9381/29/i=7/a=075004>
- 703 Coughlin, M., Harms, J., Bowden, D. C., Meyers, P., Tsai, V. C., Mandic, V., ...
704 Prestegard, T. (2019). Coherence-based approaches for estimating the compo-
705 sition of the seismic wavefield. *Journal of Geophysical Research: Solid Earth*,
706 *124*(3), 2941-2956. Retrieved from [https://agupubs.onlinelibrary.wiley](https://agupubs.onlinelibrary.wiley.com/doi/abs/10.1029/2018JB016608)
707 [.com/doi/abs/10.1029/2018JB016608](https://agupubs.onlinelibrary.wiley.com/doi/abs/10.1029/2018JB016608) doi: 10.1029/2018JB016608
- 708 Coughlin, M., Mukund, N., Harms, J., Driggers, J., Adhikari, R., & Mitra, S. (2016).
709 Towards a first design of a Newtonian-noise cancellation system for Advanced
710 LIGO. *Classical and Quantum Gravity*, *33*(24), 244001. Retrieved from
711 <http://stacks.iop.org/0264-9381/33/i=24/a=244001>
- 712 Coughlin, M. W., Harms, J., Driggers, J., McManus, D. J., Mukund, N., Ross,
713 M. P., ... Venkateswara, K. (2018, Nov). Implications of Dedicated Seis-
714 mometer Measurements on Newtonian-Noise Cancellation for Advanced LIGO.
715 *Phys. Rev. Lett.*, *121*, 221104. Retrieved from [https://link.aps.org/doi/](https://link.aps.org/doi/10.1103/PhysRevLett.121.221104)
716 [10.1103/PhysRevLett.121.221104](https://link.aps.org/doi/10.1103/PhysRevLett.121.221104) doi: 10.1103/PhysRevLett.121.221104
- 717 Dahlen, F., & Tromp, J. (1998). *Theoretical global seismology*. Princeton university
718 press.
- 719 Driggers, J. C., Harms, J., & Adhikari, R. X. (2012, November). Subtrac-
720 tion of Newtonian noise using optimized sensor arrays. *Physical Review*
721 *D*, *86*, 102001. Retrieved from [http://link.aps.org/doi/10.1103/](http://link.aps.org/doi/10.1103/PhysRevD.86.102001)
722 [PhysRevD.86.102001](http://link.aps.org/doi/10.1103/PhysRevD.86.102001) doi: 10.1103/PhysRevD.86.102001
- 723 ET Science Team. (2011). Einstein gravitational wave Telescope conceptual design
724 study. *available from European Gravitational Observatory, document number*
725 *ET-0106C-10*.
- 726 Fan, Y., & Snieder, R. (2009, November). Required source distribution for inter-
727 ferometry of waves and diffusive fields. *Geophysical Journal International*,
728 *179*(2), 1232-1244. doi: 10.1111/j.1365-246X.2009.04358.x
- 729 Fiorucci, D., Harms, J., Barsuglia, M., Fiori, I., & Paoletti, F. (2018, March).
730 Impact of infrasound atmospheric noise on gravity detectors used for astro-
731 physical and geophysical applications. *Physical Review D*, *97*, 062003. Re-
732 trieved from <https://link.aps.org/doi/10.1103/PhysRevD.97.062003> doi:
733 10.1103/PhysRevD.97.062003
- 734 Gilbert, F., & Knopoff, L. (1960). Seismic scattering from topographic irregularities.
735 *Journal of Geophysical Research*, *65*(10), 3437-3444. Retrieved from [http://](http://dx.doi.org/10.1029/JZ065i010p03437)
736 dx.doi.org/10.1029/JZ065i010p03437 doi: 10.1029/JZ065i010p03437
- 737 Giunchi, C., Di Giovanni, M., Saccorotti, G., & Naticchioni, L. (2020, May).
738 *Seismic noise characterization of the Sos Enattos Mine (Sardinia), a can-*
739 *didate site for the next generation of terrestrial gravitational waves de-*
740 *tectors*. (EGU General Assembly 2020, Online, EGU2020-9692) doi:
741 <https://doi.org/10.5194/egusphere-egu2020-9692>
- 742 Grimm, S., & Harms, J. (2020, April). Multiband Gravitational Wave Parameter Es-
743 timation: A Study of Future Detectors. *arXiv e-prints*, arXiv:2004.01434.
- 744 Gropp, W., Lusk, E., & Skjellum, A. (1994). *Using MPI, portable parallel program-*
745 *ming with the Message-Passing Interface*. Cambridge, USA: MIT Press. doi:
746 10.7551/mitpress/7056.001.0001

- 747 Hanasoge, S., Stehly, L., Nissen-Meyer, T., & Cupillard, P. (2012, December). Non-
748 linear iterative inversions for the distribution of noise sources. In *Agu fall*
749 *meeting abstracts* (Vol. 2012, p. S53C-2513).
- 750 Harms, J. (2019, October). Terrestrial gravity fluctuations. *Living Reviews in Rela-*
751 *tivity*, 22(1), 6. Retrieved from [https://doi.org/10.1007/s41114-019-0022-](https://doi.org/10.1007/s41114-019-0022-2)
752 [2](https://doi.org/10.1007/s41114-019-0022-2) doi: 10.1007/s41114-019-0022-2
- 753 Harms, J., Acernese, F., Barone, F., Bartos, I., Beker, M., van den Brand, J. F. J.,
754 ... Wand, V. (2010). Characterization of the seismic environment at the San-
755 ford Underground Laboratory, South Dakota. *Classical and Quantum Gravity*,
756 27(22), 225011. Retrieved from [http://stacks.iop.org/0264-9381/27/](http://stacks.iop.org/0264-9381/27/i=22/a=225011)
757 [i=22/a=225011](http://stacks.iop.org/0264-9381/27/i=22/a=225011)
- 758 Harms, J., Bonilla, E. L., Coughlin, M. W., Driggers, J., Dwyer, S. E., McManus,
759 D. J., ... Venkateswara, K. (2020, May). Observation of a potential future
760 sensitivity limitation from ground motion at LIGO Hanford. *Physical Re-*
761 *view D*, 101, 102002. Retrieved from [https://link.aps.org/doi/10.1103/](https://link.aps.org/doi/10.1103/PhysRevD.101.102002)
762 [PhysRevD.101.102002](https://link.aps.org/doi/10.1103/PhysRevD.101.102002) doi: 10.1103/PhysRevD.101.102002
- 763 Hild, S., Abernathy, M., Acernese, F., Amaro-Seoane, P., Andersson, N., Arun, K.,
764 ... Yamamoto, K. (2011). Sensitivity studies for third-generation gravitational
765 wave observatories. *Classical and Quantum Gravity*, 28(9), 094013. Retrieved
766 from <http://stacks.iop.org/0264-9381/28/i=9/a=094013>
- 767 Hild, S., Chelkowski, S., Freise, A., Franc, J., Morgado, N., Flaminio, R., & DeSalvo,
768 R. (2009, December). A xylophone configuration for a third-generation gravita-
769 tional wave detector. *Classical and Quantum Gravity*, 27(1), 015003. Retrieved
770 from <https://doi.org/10.1088/0264-9381/27/1/015003> doi:
771 [10.1088/0264-9381/27/1/015003](https://doi.org/10.1088/0264-9381/27/1/015003)
- 772 Hudson, J., & Knopoff, L. (1967, January). Statistical properties of rayleigh waves
773 due to scattering by topography. *Bulletin of the Seismological Society of Amer-*
774 *ica*, 57, 83-90.
- 775 Hudson, J. A. (1967). Scattered Surface Waves from a Surface Obstacle.
776 *Geophysical Journal International*, 13(4), 441-458. Retrieved from
777 <http://gji.oxfordjournals.org/content/13/4/441.abstract> doi:
778 [10.1111/j.1365-246X.1967.tb03143.x](https://doi.org/10.1111/j.1365-246X.1967.tb03143.x)
- 779 Hudson, J. A., Humphryes, R. F., Mason, I. M., & Kembhavi, V. K. (1973, Decem-
780 ber). The scattering of longitudinal elastic waves at a rough free surface. *Jour-*
781 *nal of Physics D Applied Physics*, 6(18), 2174-2186. doi: 10.1088/0022-3727/6/
782 18/303
- 783 Hughes, S. A., & Thorne, K. S. (1998, November). Seismic gravity-gradient noise in
784 interferometric gravitational-wave detectors. *Physical Review D*, 58, 122002.
785 Retrieved from <http://link.aps.org/doi/10.1103/PhysRevD.58.122002>
786 doi: 10.1103/PhysRevD.58.122002
- 787 Komatitsch, D. (2004, February). Simulations of Ground Motion in the Los Ange-
788 les Basin Based upon the Spectral-Element Method. *The Bulletin of the Seis-*
789 *mological Society of America*, 94(1), 187-206. doi: 10.1785/0120030077
- 790 Komatitsch, D., Labarta, J., & Michéa, D. (2008). A simulation of seismic wave
791 propagation at high resolution in the inner core of the Earth on 2166 proces-
792 sors of MareNostrum. *Lecture Notes in Computer Science*, 5336, 364-377. doi:
793 [10.1007/978-3-540-92859-1_33](https://doi.org/10.1007/978-3-540-92859-1_33)
- 794 Komatitsch, D., & Martin, R. (2007, January). An unsplit convolutional perfectly
795 matched layer improved at grazing incidence for the seismic wave equation.
796 *Geophysics*, 72(5), SM155. doi: 10.1190/1.2757586
- 797 Komatitsch, D., & Tromp, J. (1999). Introduction to the spectral element method
798 for three-dimensional seismic wave propagation. *Geophysical Journal Interna-*
799 *tional*, 139(3), 806-822. Retrieved from [http://dx.doi.org/10.1046/j.1365-](http://dx.doi.org/10.1046/j.1365-246x.1999.00967.x)
800 [246x.1999.00967.x](http://dx.doi.org/10.1046/j.1365-246x.1999.00967.x) doi: 10.1046/j.1365-246x.1999.00967.x
- 801 Komatitsch, D., & Tromp, J. (2002a). Spectral-element simulations of global seis-

- mic wave propagation I. Validation. *Geophysical Journal International*, 149(2), 390-412. Retrieved from <http://gji.oxfordjournals.org/content/149/2/390.abstract> doi: 10.1046/j.1365-246X.2002.01653.x
- Komatitsch, D., & Tromp, J. (2002b). Spectral-element simulations of global seismic wave propagation—ii. three-dimensional models, oceans, rotation and self-gravitation. *Geophysical Journal International*, 150(1), 303-318. Retrieved from <https://onlinelibrary.wiley.com/doi/abs/10.1046/j.1365-246X.2002.01716.x> doi: 10.1046/j.1365-246X.2002.01716.x
- Komatitsch, D., Tsuboi, S., Ji, C., & Tromp, J. (2003, November). A 14.6 billion degrees of freedom, 5 teraflops, 2.5 terabyte earthquake simulation on the Earth Simulator. In *Proceedings of the sc'03 acm/ieee conference on supercomputing* (p. 4-11). Phoenix, Arizona, USA: ACM. (Gordon Bell Prize winner article) doi: 10.1145/1048935.1050155
- Komatitsch, D., & Vilotte, J.-P. (1998). The spectral element method: An efficient tool to simulate the seismic response of 2D and 3D geological structures. *Bulletin of the Seismological Society of America*, 88(2), 368-392. Retrieved from <http://www.bssaonline.org/content/88/2/368.abstract>
- Komatitsch, D., Vilotte, J.-P., Afanasiev, M., Ampuero, J.-P., Bachmann, E., Bai, K., ... Zhu, H. (2018). *Specfem 3d cartesian v3.0 [software]*.
- Komatitsch, D., Vilotte, J.-P., Vai, R., Castillo-Covarrubias, J. M., & Sánchez-Sesma, F. J. (1999, July). The spectral element method for elastic wave equations—application to 2-D and 3-D seismic problems. *International Journal for Numerical Methods in Engineering*, 45(9), 1139-1164. doi: 10.1002/(SICI)1097-0207(19990730)45:9<1139::AID-NME617>3.0.CO;2-T
- Liu, Q., & Tromp, J. (2006, December). Finite-Frequency Kernels Based on Adjoint Methods. *The Bulletin of the Seismological Society of America*, 96(6), 2383-2397. doi: 10.1785/0120060041
- Liu, Q., & Tromp, J. (2008, July). Finite-frequency sensitivity kernels for global seismic wave propagation based upon adjoint methods. *Geophysical Journal International*, 174(1), 265-286. doi: 10.1111/j.1365-246X.2008.03798.x
- Lobkis, O. I., & Weaver, R. L. (2001). On the emergence of the Green's function in the correlations of a diffuse field. *The Journal of the Acoustical Society of America*, 110(6), 3011-3017. Retrieved from <https://doi.org/10.1121/1.1417528> doi: 10.1121/1.1417528
- Maday, Y., & Patera, A. T. (1989, January). Spectral element methods for the incompressible Navier-Stokes equations. In *In: State-of-the-art surveys on computational mechanics (a90-47176 21-64)*. new york (p. 71-143).
- Maggiore, M., Broeck, C. V. D., Bartolo, N., Belgacem, E., Bertacca, D., Bizouard, M. A., ... Sakellariadou, M. (2020, March). Science case for the einstein telescope. *Journal of Cosmology and Astroparticle Physics*, 2020(03), 050–050. Retrieved from <https://doi.org/10.1088/1475-7516/2020/03/050> doi: 10.1088/1475-7516/2020/03/050
- Mandic, V., Tsai, V. C., Pavlis, G. L., Prestegard, T., Bowden, D. C., Meyers, P., & Caton, R. (2018). A 3D Broadband Seismometer Array Experiment at the Homestake Mine. *Seismological Research Letters*, 89(6), 2420. Retrieved from <http://dx.doi.org/10.1785/0220170228> doi: 10.1785/0220170228
- Maradudin, A., & Mills, D. (1976, September). Attenuation of rayleigh surface waves by surface roughness. *Annals of Physics*, 100, 262-309. doi: 10.1016/0003-4916(76)90063-4
- Martin, R., & Komatitsch, D. (2009, October). An unsplit convolutional perfectly matched layer technique improved at grazing incidence for the viscoelastic wave equation. *Geophysical Journal International*, 179(1), 333-344. doi: 10.1111/j.1365-246X.2009.04278.x
- Martin, R., Komatitsch, D., Gedney, S., & Bruthiaux, E. (2010, January). A high-order time and space formulation of the unsplit perfectly matched layer

- 857 for the seismic wave equation using auxiliary differential equations (ade-
858 pml). *Computer Modelling in Engineering and Sciences - CMES*, 56. doi:
859 10.3970/cmcs.2010.056.017
- 860 Matchard, F., Lantz, B., Mason, K., Mittleman, R., Abbott, B., Abbott, S., ...
861 Warner, J. (2014). Advanced LIGO two-stage twelve-axis vibration isolation
862 and positioning platform. Part 1: Design and production overview. *Preci-
863 sion Engineering*(0), -. Retrieved from [http://www.sciencedirect.com/
864 science/article/pii/S0141635914001561](http://www.sciencedirect.com/science/article/pii/S0141635914001561) doi: [http://dx.doi.org/10.1016/
865 j.precisioneng.2014.09.010](http://dx.doi.org/10.1016/j.precisioneng.2014.09.010)
- 866 Montagner, J.-P., Larmat, C., Capdeville, Y., Fink, M., Phung, H., Romanowicz,
867 B., ... Kawakatsu, H. (2012, 11). Time-reversal method and cross-correlation
868 techniques by normal mode theory: a three-point problem. *Geophysical Jour-
869 nal International*, 191(2), 637-652. Retrieved from [https://doi.org/10
870 .1111/j.1365-246X.2012.05619.x](https://doi.org/10.1111/j.1365-246X.2012.05619.x) doi: 10.1111/j.1365-246X.2012.05619.x
- 871 Mooney, H. M. (1976). The seismic wave system from a surface impact. *Geophysics*,
872 41(2), 243-265. Retrieved from [http://geophysics.geoscienceworld.org/
873 content/41/2/243.abstract](http://geophysics.geoscienceworld.org/content/41/2/243.abstract) doi: 10.1190/1.1440614
- 874 Ogilvy, J. A. (1987). Wave scattering from rough surfaces. *Reports on Progress in
875 Physics*, 50(12), 1553. Retrieved from [http://stacks.iop.org/0034-4885/
876 50/i12/a12](http://stacks.iop.org/0034-4885/50/i12/a12) doi: 10.1088/0034-4885/50/12/001
- 877 Olsen, K. B., Madariaga, R., & Archuleta, R. J. (1997, October). Three-Dimensional
878 Dynamic Simulation of the 1992 Landers Earthquake. *Science*, 278, 834-838.
879 doi: 10.1126/science.278.5339.834
- 880 Orfanidis, S. J. (2007). *Optimum signal processing: an introduction*. Macmillan pub-
881 lishing company.
- 882 Otto, O. W. (1977, December). Scattering of Rayleigh waves from topographic irreg-
883 ularities at oblique incidence. *Journal of Applied Physics*, 48(12), 5105-5110.
884 doi: 10.1063/1.323587
- 885 Pacheco, P. S. (1997). *Parallel programming with MPI*. San Francisco, USA: Morgan
886 Kaufmann Press.
- 887 Patera, A. T. (1984, June). A Spectral Element Method for Fluid Dynamics: Lam-
888 inar Flow in a Channel Expansion. *Journal of Computational Physics*, 54(3),
889 468-488. doi: 10.1016/0021-9991(84)90128-1
- 890 Peter, D., Komatitsch, D., Luo, Y., Martin, R., Le Goff, N., Casarotti, E., ...
891 Tromp, J. (2011). Forward and adjoint simulations of seismic wave propa-
892 gation on fully unstructured hexahedral meshes. *Geophysical Journal Interna-
893 tional*, 186(2), 721-739. doi: 10.1111/j.1365-246X.2011.05044.x
- 894 Peter, D., Tape, C., Boschi, L., & Woodhouse, J. H. (2007, December). Surface wave
895 tomography: global membrane waves and adjoint methods. *Geophysical Jour-
896 nal International*, 171(3), 1098-1117. doi: 10.1111/j.1365-246X.2007.03554.x
- 897 Punturo, M., Abernathy, M., Acernese, F., Allen, B., Andersson, N., Arun, K., ...
898 Yamamoto, K. (2010). The Einstein Telescope: a third-generation gravita-
899 tional wave observatory. *Classical and Quantum Gravity*, 27(19), 194002.
900 Retrieved from <http://stacks.iop.org/0264-9381/27/i=19/a=194002>
- 901 Reitze, D., Adhikari, R. X., Ballmer, S., Barish, B., Barsotti, L., Billingsley, G., ...
902 Zucker, M. (2019, September). Cosmic Explorer: The U.S. Contribution to
903 Gravitational-Wave Astronomy beyond LIGO. In *Bulletin of the american
904 astronomical society* (Vol. 51).
- 905 Sanchez-Sesma, F., & Campillo, M. (1991, January). Diffraction of p, sv and
906 rayleigh waves by topographic features: a boundary integral formulation. *Bul-
907 letin - Seismological Society of America*, 81(6), 2234-2253.
- 908 Sathyaprakash, B., Abernathy, M., Acernese, F., Ajith, P., Allen, B., Amaro-
909 Seoane, P., ... Yamamoto, K. (2012). Scientific objectives of einstein tele-
910 scope. *Classical and Quantum Gravity*, 29(12), 124013. Retrieved from
911 <http://stacks.iop.org/0264-9381/29/i=12/a=124013>

- 912 Seriani, G., & Priolo, E. (2012, December). Spectral element method for acoustic
 913 wave simulation in heterogeneous media. *Finite Elements in Analysis and De-*
 914 *sign*, *16*, 337-348. doi: 10.1016/0168-874X(94)90076-0
- 915 Snieder, R. (1986, November). The influence of topography on the propagation
 916 and scattering of surface waves. *Physics of the Earth and Planetary Interiors*,
 917 *44*(3), 226-241. doi: 10.1016/0031-9201(86)90072-5
- 918 Souradeep, T. (2016). LIGO-India. *Resonance*, *21*, 225 – 231. Retrieved
 919 from <https://doi.org/10.1007/s12045-016-0316-6> doi: 10.1007/
 920 s12045-016-0316-6
- 921 Tromp, J., Komatitsch, D., & Liu, Q. (2008). Spectral-element and adjoint methods
 922 in seismology. *Communications in Computational Physics*, *3*(1), 1-32.
- 923 Tromp, J., Luo, Y., Hanasoge, S., & Peter, D. (2010, November). Noise cross-
 924 correlation sensitivity kernels. *Geophysical Journal International*, *183*(2),
 925 791-819. doi: 10.1111/j.1365-246X.2010.04721.x
- 926 Tromp, J., Tape, C., & Liu, Q. (2005, January). Seismic tomography, adjoint meth-
 927 ods, time reversal and banana-doughnut kernels. *Geophysical Journal Interna-*
 928 *tional*, *160*(1), 195-216. doi: 10.1111/j.1365-246X.2004.02453.x
- 929 Tsai, V. C., & Moschetti, M. P. (2010, July). An explicit relationship be-
 930 tween time-domain noise correlation and spatial autocorrelation (SPAC)
 931 results. *Geophysical Journal International*, *182*(1), 454-460. doi: 10.1111/
 932 j.1365-246X.2010.04633.x
- 933 Tsuboi, S., Komatitsch, D., Ji, C., & Tromp, J. (2003, October). Broadband model-
 934 ing of the 2002 Denali fault earthquake on the Earth Simulator. *Physics of the*
 935 *Earth and Planetary Interiors*, *139*(3-4), 305-313. doi: 10.1016/j.pepi.2003.09
 936 .012
- 937 Virieux, J. (1986, April). P-SV wave propagation in heterogeneous media: Velocity-
 938 stress finite-difference method. *Geophysics*, *51*(4), 889-901. doi: 10.1190/
 939 .1442147
- 940 Wapenaar, K., Slob, E., & Snieder, R. (2006, December). Unified Green's Function
 941 Retrieval by Cross Correlation. *Physical Review Letters*, *97*(23), 234301. doi:
 942 10.1103/PhysRevLett.97.234301
- 943 Woodard, M. F. (1997, August). Implications of Localized, Acoustic Absorption
 944 for Heliotomographic Analysis of Sunspots. *The Astrophysical Journal*, *485*(2),
 945 890-894. doi: 10.1086/304468
- 946 Woods, R. D. (1968). Screening of Surface Waves in Soils. *Journal of the Soil Me-*
 947 *chanics and Foundations Division: proceedings of the American Society of Civil*
 948 *Engineers*, *94*(4), 951-979.
- 949 Xie, Z., Komatitsch, D., Martin, R., & Matzen, R. (2014, September). Improved for-
 950 ward wave propagation and adjoint-based sensitivity kernel calculations using
 951 a numerically stable finite-element PML. *Geophysical Journal International*,
 952 *198*(3), 1714-1747. doi: 10.1093/gji/ggu219